Fall 2022

ACCURACY IMPROVEMENT OF CABLE HARNESS MODELING & ANALYTICAL MODELING OF MULTI-REFLECTIONS IN HIGH-SPEED SIGNAL CHANNELS

Muqi Ouyang
Missouri University of Science and Technology

Department: Electrical and Computer Engineering

Recommended Citation

Ouyang, Muqi, "ACCURACY IMPROVEMENT OF CABLE HARNESS MODELING & ANALYTICAL MODELING OF MULTI-REFLECTIONS IN HIGH-SPEED SIGNAL CHANNELS" (2022). *Doctoral Dissertations*. 3229.
https://scholarsmine.mst.edu/doctoral_dissertations/3229

ACCURACY IMPROVEMENT OF CABLE HARNESS MODELING & ANALYTICAL MODELING OF MULTI-REFLECTIONS IN HIGH-SPEED SIGNAL CHANNELS

by

MUQI OUYANG

A DISSERTATION

Presented to the Graduate Faculty of the

MISSOURI UNIVERSITY OF SCIENCE AND TECHNOLOGY

In Partial Fulfillment of the Requirements for the Degree

DOCTOR OF PHILOSOPHY

in

ELECTRICAL ENGINEERING

2022

Approved by:

Chulsoon Hwang, Advisor
Jun Fan, Co-Advisor
DongHyun(Bill) Kim
James L. Drewniak
Xiaoming He

PUBLICATION DISSERTATION OPTION

This dissertation consists of the following three articles, formatted in the style used by the Missouri University of Science and Technology:

Paper I, found on pages 3–37, “Novel Formulations of Multireflections and Their Applications to High-Speed Channel Design,” has been published by *IEEE Transaction on Signal and Power Integrity* in May 2022.

Paper II, found on pages 38–53, “Improvement of Convergence Characteristics in the Generalized Multiconductor Transmission-Line Method Near Resonant Frequencies,” is intended for submission to *IEEE Transaction on Electromagnetic Compatibility*.

Paper III, found on pages 54–87, “An Improvement on the Multiple Scattering Method for Evaluating Current Distributions on Cable Harness Using the Sub-Structure Analysis,” is intended for submission to *IEEE Transaction on Electromagnetic Compatibility*.

ABSTRACT

Cable harnesses are widely used in modern vehicles to power electric systems locating at different locations throughout the vehicle and to establish signal channels for data communications between these systems. Generally, a cable harness consists of multiple wires and its geometry can be very complicated, making full-wave modeling and simulation approaches computational resource-intensive. To cut down the computational effort, the hybrid multiconductor transmission-line (MTL) method has been developed, and the generalized MTL (GMTL) method and the multiple scattering (MS) method have been developed to improve the accuracy of the hybrid MTL method. In this research, the convergence issue in the GMTL method near the resonant frequencies of a cable harness system is analyzed, and the solution to improve the convergence characteristics near resonant frequencies is proposed. Also, the MS method has been improved by simplifying the steps of iterative calculations with sub-structure analysis.

In high-speed signal channels, the signal reflections resulting from the discontinuities of characteristic impedances can be the major contributor to the degraded signal quality. In this research, the closed-form formulations to calculate the wave propagations and reflections in a cascaded channel with impedance discontinuities have been developed. With the developed formulations, the propagation paths for each individual ripple in the channel's single-bit response (SBR) can be backtracked. After identifying the critical ripples in SBR that are responsible for the channel's degraded signal quality and their propagation paths, the most effective and practical solutions for channel optimization can be determined.

ACKNOWLEDGMENTS

First, I would like to express my most sincere gratitude to my advisor, Dr. Chulsoon Hwang, and my co-advisor, Dr. Jun Fan. I've started working with Dr. Hwang and Dr. Fan as an undergraduate intern and I really appreciated the opportunity they offered to me to pursue my Ph.D. degree in their group. In the beginning years of my Ph.D. program, I was fresh to everything, and they were really patient to help me start my research work and to encourage me not to give up when facing challenges. My work in this dissertation would not have been possible without their support.

I would like to thank Dr. DongHyun(Bill) Kim for all the guidance, suggestions, and helpful discussions in my research work.

I would like to thank Dr. James Drewniak for his lectures and his suggestions and encourgements on my research works.

I would like to thank Dr. Xiaoming He for his lectures on numerical analysis and providing suggestions and comments from the mathematical aspects. What I learned in his lectures was very helpful for me to complete my dissertation work.

Also, thanks are also due to all the faculty members, students, and friends in our EMC Laboratory at Missouri S&T. I was helped a lot on my research and course work, and I really enjoyed working together with you in our lab.

Finally, I would like to thank my parents for their unconditional support in all aspects during my pursuit to my Ph.D. degree.

The work in this dissertation was supported in part by the National Science Foundation under Grant No. IIP-1916535.

TABLE OF CONTENTS

Page

SECTION

PAPER

SECTION

LIST OF ILLUSTRATIONS

PAPER I Page

PAPER II

PAPER III

LIST OF TABLES

PAPER I Page

PAPER II

PAPER III

1. INTRODUCTION

Cable harness has been widely used in many complex systems such as vehicles, high-speed trains, and airplanes, where many sensitive equipments are put together in a single system and are connected with cable harness. Therefore, evaluating the current distributions on cable harness accurately and efficiently in a complex system is important to analyze the electromagnetic fields radiated out from the harness or incident to the harness to avoid potential electromagnetic interference (EMI) problems in a complex system.

Generally, there can be many wires in a single cable harness bundle. So using full-wave algorithms like finite element method (FEM) or method of moment (MoM) to solve a cable harness problem requires solving matrix equations with large dimensions because the complex cable harness geometries will result in many meshes. To cut down the required computational resources when solving the cable harness problem, many algorithms have been developed, including the generalized MTL method and the Multiple Scattering method. An improvement has been made on the generalized MTL method to improve the convergence characteristics near the resonant frequencies of the cable harness system. In addition, the Multiple Scattering method is improved with the help of sub-structure analysis method. The iterative steps in the Multiple Scattering method are simplified and less complicated iterative calculations are required in the improved Mulitple Scattering method.

In high-speed signal channels, the characteristic impedance discontinuities together with the insertion loss and the crosstalk are the most critical issues, and the analysis and optimizations focusing on the characteristic impedance discontinuities are studied. Analytical formulations for a cascaded channel with impedance discontinuities are derived from the transmissions and reflections of wave components in the cascaded channel. Using the derived analytical formulations, each wave components received at the received side can be backtracked. Therefore, by identifying the critical wave components at the receiver and backtracking their propagation paths, more specific solutions for channel optimization can be determined, and the channel optimization process can be more efficient.

PAPER

I. NOVEL FORMULATIONS OF MULTI-REFLECTIONS AND THEIR APPLICATIONS TO HIGH-SPEED CHANNEL DESIGN

ABSTRACT

Reflection theory has been long established for over decades targeted at microwave and radio frequency (RF) applications. With ultra-high-bandwidth applications emerging, such as 112Gb/s and higher speed Ethernet protocols, discontinuities in high-speed channels negatively impact signal quality, where reflections become one of the most critical concerns in high-speed designs. In this paper, for the first time, we analyzed the traditional reflection theory and proposed and verified a new formulation, which exhibits the reflection-related parameters explicitly, indicating where design optimization can be made for high bandwidth applications using the backtracked propagation method. Our closed-form formulation is applied to high-speed channel examples, where effective mitigation of negative impact from reflections on signal integrity can be identified to be used as a pre-layout channel design guide. Our proposed formulation of the reflection theory provides more accurate prediction of high-speed channel behavior to minimize the negative signal integrity impact from reflections.

Keywords: Eye diagram, High-speed channel, Multi-reflections, Signal integrity.

1. INTRODUCTION

High-speed channels up to 112Gb/s are widely used in industry protocols, commercialized through computer and communication equipment. Even though much higher speeds (224 Gb/s and above) are being conceived with cable (copper and optical) solutions, concurrent interconnections are still primarily implemented on PCBs [1]. At higher speeds, signal reflections in the channels become more severe than before due to unavoidable characteristic impedance discontinuities, in packages, connectors, pin fields, and transition vias [2, 3]. Because of low-loss materials being used for most high-speed channels for the purpose of decreasing insertion losses, reflections in the form of multi-reflection become more pronounced, leading to a primary cause for channel failures [4].

The conventional high-speed design would resort to full-wave modeling and simulation tools, which require high computational resource and time, producing desired channel performance in many cases. However, this traditional design approach may obscure the reflection mechanisms, leading designers not to know where a potential problem exists and how to solve it. As the complexity of PCB designs increases, component placement and PCB layout become a sensitive and critical process, determining the signal integrity of the high-speed channels. In the past, component placement may be flexible with few considerations for the reflections. With the unprecedented higher speeds, a slight displacement of a critical component may incur an unforeseen channel quality disturbance, which leaves a little clue of disturbance source to the channel designers [5].

There are three major technical obstacles for high-speed signals regarding inter-chassis and within chassis transmissions: insertion loss, return loss, and crosstalk [4, 6]. The insertion loss issues have been mainly solved by using low loss and ultra-loss materials upon proper equalization schemes. At the same time, crosstalk concerns can be mitigated by appropriate layout and spacing. The more challenging issue is return loss, which may be only solved by advanced equalization techniques. However, it is possible that there may be ways to lower the return losses with less power consumption and lower chip development costs. Theoretically, the reflection theory can explain the intricacies embedded in the channel return losses, which can lead to a technical insight on how reflection can be minimized without additional active solutions.

Reflection theory has been developed with radio frequency (RF) and microwave engineering for many decades [7], mainly limited to addressing bandlimited applications. Its applications to the high speed and high bandwidth signal transmission emerged about 30 years ago when data rates increased to the Gb/s ranges for inter-chassis and within chassis communications. For instance, the first generation of PCI Express started operating at 2.5Gb/s less than two decades ago. Since then, a few industry protocols, including Ethernet, SAS, SATA, and Infiniband, began increasing the bandwidth with a multiplier for every new generation. When Ethernet's data rates increased to the 100Gb/s range, high-speed signals have become truly super wideband from DC to their fundamental frequencies with lower-order harmonics spanning to their speed ranges in GHz [8].

With much higher data rates emerging in concurrent communication protocols, signal quality must be guaranteed in the wide frequency ranges without intolerable degradations, which imposes stringent requirements for understanding the reflection mechanisms. High-speed channels used in digital data communication are different from the ones used in the RF and microwave applications with the following features:

1. Multiple PCBs with sizable dimensions
2. Hybrid connection with connectors and cables
3. Cascaded interconnections with different system reference impedances
4. Long transmission distance
5. Thick PCB boards with up to dozens of layers
6. Multiple channels running in close vicinity
7. Discontinuities are separated from small to large distances along the transmission lines
8. Involving discrete passive components such as DC block capacitors and transition vias

All the above physical features must satisfy the same signal condition – ultra-high bandwidth. Traditional reflection theory may seem inadequate to be applied to all the above attributes for the concerned high-speed channels.

In this paper, we analyzed the reflection theory and reformulated the reflection mechanisms with a couple of new proposals targeted at the concerned high-speed channels specifically [9-12]. We proposed a new insertion loss formulation with reflected components represented explicitly, indicating how multi-reflection impacts the received signal quality in a closed-form fashion [13]. To reveal the multi-reflection happening between different interfaces formed by interconnecting components modeled with S-parameters, two theoretical methods were created to quantitatively account for the reflected waves explicitly. As a validation of our unique formulations, we compared our results with those generated from commercial tools, which confirms the accuracy of our theory.

The second part of this paper shows application of our newly proposed formulations to high-speed channel optimization. Channel optimization on reflection-related structures has special and immediate effects if performed correctly. Reflection-related structures in a normal high-speed channel are those with impedances different from what the system specifies or those with poor return loss modeled separately, also called discontinuity structures. High-impacting discontinuity structures may include vias and pins in series connection with the high-speed channels, directly degrading signal quality.

In this paper, we propose a set of approaches that enable optimizing the distributed discontinuities in a high-speed channel. We tackle two different problems through our approaches: optimizing the distance between discontinuities and optimizing the reflections in the transmission lines based on our closed-form formulations. Our optimization targets are the minimized ripples seen at the receiver and the improved eye opening in eye diagrams, respectively, with our proposed approaches. Our results have been verified with commercial tools, confirming with high confidence.

The organization of this paper is briefly summarized here. In Section II, the derivations on the closed-form formulations are discussed based on the multi-reflections in cascaded channels, and two methods to handle cascaded S-parameter networks are also proposed. In Section III, the accuracy of the derived formulations is validated using a numerical example. In Section IV, the methods to optimize cascaded channels are discussed based on practical channel configurations: 3 segments of PCB striplines with 2 via transition structures. In Section V, discussions and conclusions of this paper are given.

2. CLOSED-FORM FORMULATIONS

The derivation of the closed-form formulations for the insertion loss $S_{21}(\omega)$ and the group delay $t_g(\omega)$ of a single-ended cascaded channel have been discussed in detail in [13]. In the cascaded channel, each segment is modeled using a frequency-dependent PCB stripline model. In this section, the formulation derivation is reviewed briefly, and the formulations are extended to handle more practical cases: differential channels with cascaded S-parameter networks.

2.1. FREQUENCY-DEPENDENT PARAMETERS FOR PCB STRIPLINES

The solutions for frequency-dependent RLGC parameters for both single-ended and differential PCB striplines are introduced in [14], and the formulations for RLGC parameters from PCB cross-sectional geometries are also presented below.

The free-space permittivity and permeability are represented as ε_0 and μ_0, accordingly. The relative permittivity of the PCB dielectric is represented as $\varepsilon_r(\omega)$, which is frequency-dependent and complex. To ensure the causality of the system, the Djordjevic model for $\varepsilon_r(\omega)$ is implemented [15]:

$$\varepsilon_r(\omega) = \varepsilon_\infty + a \cdot \ln\left(\frac{2\pi f_H + j \cdot \omega}{2\pi f_L + j \cdot \omega}\right) \tag{1}$$

where ε_∞ is the real relative permittivity value when $\omega \to \infty$; a is a constant factor; f_L and f_H are the pre-defined lower and upper frequency limitations. By defining the real part of the relative permittivity $\varepsilon'_{r,\omega_0}$ and the loss tangent $\tan\delta_{\omega_0}$ at a certain frequency ω_0, the complex relative permittivity $\varepsilon_r(\omega_0)$ at frequency ω_0 can be written as:

$$\varepsilon_r(\omega_0) = \varepsilon'_{r,\omega_0} - j \cdot \varepsilon'_{r,\omega_0} \cdot \tan\delta_{\omega_0} \tag{2}$$

Then the unknown constant in the Djordjevic model ε_∞ and a can be solved by:

$$\begin{cases} a = -\dfrac{\varepsilon'_{r,\omega_0} \cdot \tan\delta_{\omega_0}}{\mathrm{Imag}\left\{\ln\left(\dfrac{2\pi f_H + j \cdot \omega}{2\pi f_L + j \cdot \omega}\right)\right\}} \\ \varepsilon_\infty = \varepsilon'_{r,\omega_0} + \varepsilon'_{r,\omega_0} \cdot \tan\delta_{\omega_0} \cdot \dfrac{\mathrm{Real}\left\{\ln\left(\dfrac{2\pi f_H + j \cdot \omega}{2\pi f_L + j \cdot \omega}\right)\right\}}{\mathrm{Imag}\left\{\ln\left(\dfrac{2\pi f_H + j \cdot \omega}{2\pi f_L + j \cdot \omega}\right)\right\}} \end{cases} \tag{3}$$

For a single-ended symmetrical PCB stripline, the cross-sectional geometry is shown in Figure 1. W and t are the width and thickness of the metal trace; b is the total thickness of the PCB dielectric; ρ is the resistance of the metal material; $G_p = 1.5$ is the factor related to the conductor loss contributed by the current in the ground plane for symmetrical striplines.

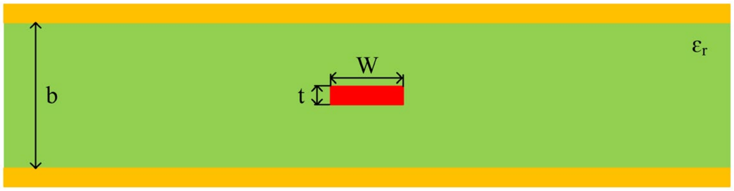

Figure 1. Cross-sectional geometry of a single-ended symmetrical stripline.

When $W \gg t$, the skin-effect onset frequency is defined as:

$$f_{surf} = \frac{4\rho}{t^2 \pi \mu_0} \tag{4}$$

Then, the frequency-dependent RLGC parameters for the single-ended stripline are:

$$\begin{cases} R_{se}(\omega) = \dfrac{\rho}{Wt} + \dfrac{\rho G_p}{Wt\sqrt{2\pi f_{surf}}}\sqrt{\omega} \\ L_{se}(\omega) = Z_{SE}\sqrt{\mu_0 \varepsilon_0 \varepsilon_r} + \dfrac{\rho G_p}{Wt\sqrt{2\pi f_{surf}}} \cdot \dfrac{1}{\sqrt{\omega}} \\ G_{se}(\omega) = \omega \dfrac{\varepsilon_r''}{\varepsilon_r} \cdot \dfrac{\sqrt{\mu_0 \varepsilon_0 \varepsilon_r}}{Z_{SE}} \\ C_{se}(\omega) = \dfrac{\varepsilon_r'}{\varepsilon_r} \cdot \dfrac{\sqrt{\mu_0 \varepsilon_0 \varepsilon_r}}{Z_{SE}} \end{cases} \tag{5}$$

where

$$Z_{SE} = \frac{30\pi(b-t)}{\sqrt{\varepsilon_r}\left(W + \dfrac{bC_f}{\pi}\right)} \tag{5a}$$

$$C_f = 2\,ln\left(\frac{2b-t}{b-t}\right) - \frac{t}{b}\,ln\left[\frac{t(2b-t)}{(b-t)^2}\right] \tag{5b}$$

The cross-sectional geometry of a differential symmetrical PCB stripline is shown in Figure 2. In addition to the single-ended stripline cross-section, the spacing between the 2 signal conductors is defined as s.

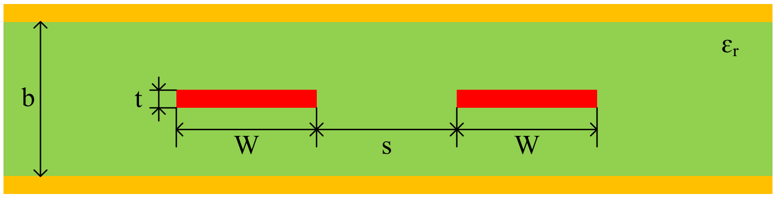

Figure 2. Cross-sectional geometry of a differential symmetrical stripline.

To investigate the signal propagations and reflections in differential channels, the focus should be on the odd-mode characteristics of the system. Similar to the single-ended RLGC parameters, the odd-mode RLGC parameters of a differential stripline can be written as:

$$\begin{cases} R_{odd}(\omega) = \dfrac{\rho}{Wt} + \dfrac{\rho G_p}{Wt\sqrt{2\pi f_{surf}}}\sqrt{\omega} \\ L_{odd}(\omega) = Z_{ODD}\sqrt{\mu_0 \varepsilon_0 \varepsilon_r} + \dfrac{\rho G_p}{Wt\sqrt{2\pi f_{surf}}} \cdot \dfrac{1}{\sqrt{\omega}} \\ G_{odd}(\omega) = \omega \dfrac{\varepsilon_r''}{\varepsilon_r} \cdot \dfrac{\sqrt{\mu_0 \varepsilon_0 \varepsilon_r}}{Z_{ODD}} \\ C_{odd}(\omega) = \dfrac{\varepsilon_r'}{\varepsilon_r} \cdot \dfrac{\sqrt{\mu_0 \varepsilon_0 \varepsilon_r}}{Z_{ODD}} \end{cases} \tag{6}$$

where

$$Z_{ODD} = \frac{30\pi(b-t)}{\sqrt{\varepsilon_r}\left[W + \dfrac{bC_{f,odd}}{2\pi}\left(1 + \dfrac{\ln[1 + tanh(\theta)]}{\ln(2)}\right)\right]} \tag{6a}$$

and

$$C_{f,odd} = 2\,ln\left(\frac{2b-t}{b-t}\right) - \frac{t}{b}ln\left[\frac{t(2b-t)}{(b-t)^2}\right];\ \theta = \frac{\pi s}{2b} \tag{6b}$$

For both the single-ended and the odd mode in the differential systems, the frequency-dependent characteristic impedance $Z_C(\omega)$ and the propagation constant $\gamma(\omega)$ can be calculated using $RLGC_{se}(\omega)$ and $RLGC_{odd}(\omega)$, respectively:

$$Z_C(\omega) = \sqrt{\frac{R(\omega) + j\omega L(\omega)}{G(\omega) + j\omega C(\omega)}} \tag{7}$$

$$\gamma(\omega) = \sqrt{[R(\omega) + j\omega L(\omega)] \cdot [G(\omega) + j\omega C(\omega)]} \tag{8}$$

Then, the signal reflections and transmissions at the interfaces between different segments and the signal propagations inside each segment in the cascaded channel can be evaluated using the derived frequency-dependent $Z_C(\omega)$ and $\gamma(\omega)$.

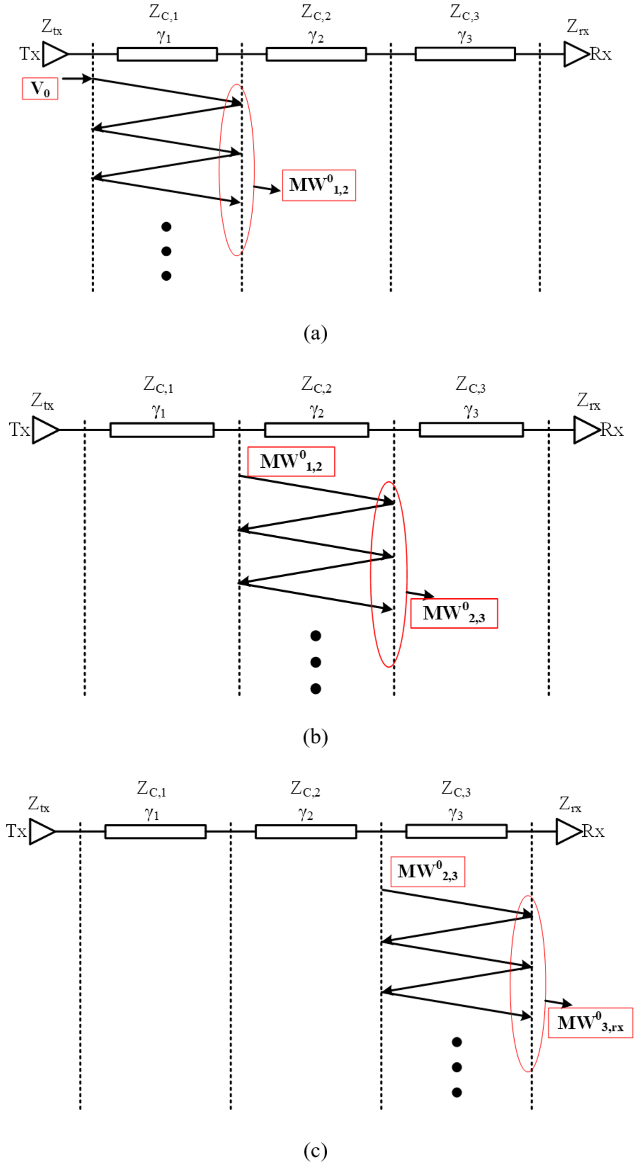

(a)

(b)

(c)

Figure 3. An example of 3 cascaded striplines and wave propagations and reflections in (a) the 1st stripline; (b) the 2nd stripline; and (c) the 3rd stripline.

2.2. A CASCADED CHANNEL WITH TRANSMISSION-LINE SEGMENTS

For both the single-ended and the differential systems with cascaded transmission-line segments, the method presented in [13] can be used to derive the closed-form formulations for the insertion loss $S_{21}(\omega)$ of the system.

In Figure 3, a cascaded channel with 3 stripline segments and the wave propagations and reflections in each individual segment is shown.

$Z_{C,i}$ and γ_i $(i = 1, 2, 3)$ are the characteristic impedances and the propagation constants of each segment of stripline, and the lengths of striplines are l_1, l_2 and l_3. Z_{tx} and Z_{rx} are the impedances of the transmitter and the receiver. The wave incident from the transmitter to the 1st stripline segment is V_0, and $MW_{i,j}^{0}$ indicates the group of multiple waves incident from stripline segment i to stripline segment j. The transmission coefficient and the reflection coefficient from the stripline segment i to the stripline segment j are:

$$\mathrm{T}_{i,j}(\omega) = \frac{2Z_{C,j}(\omega)}{Z_{C,j}(\omega) + Z_{C,i}(\omega)} \tag{9}$$

$$\Gamma_{i,j}(\omega) = \frac{Z_{C,j}(\omega) - Z_{C,i}(\omega)}{Z_{C,j}(\omega) + Z_{C,i}(\omega)} \tag{10}$$

Notice that both the transmission coefficients and reflection coefficients defined in (9) and (10) have a directional indication. To simplify the formulation writing, for a cascaded channel with N segments, let the subscript i or j represent the transmitter or the receiver when the value is 0 or $N + 1$, respectively. For example, $Z_{C,0} = Z_{tx}$, $Z_{C,N+1} = Z_{rx}$, $\mathrm{T}_{0,1} = \mathrm{T}_{tx,1}$, $\mathrm{T}_{N+1,N} = \mathrm{T}_{rx,N}$, $\Gamma_{1,0} = \Gamma_{1,tx}$, $\Gamma_{N,N+1} = \Gamma_{N,rx}$ and $MW_{N,N+1} = MW_{N,rx}$. In (9) and (10), $i = 0,1, \dots, N + 1$, $j = 0,1, \dots, N + 1$, and $i \neq j$.

Then, the wave incident from the 1st stripline to the 2nd stripline is

$$
\begin{aligned}
MW_{1,2}^{0}(M) &= V_0 \mathrm{T}_{tx,1}\mathrm{T}_{1,2}e^{-\gamma_1 l_1}\left(1+\Gamma_{1,2}\Gamma_{1,tx}e^{-2\gamma_1 l_1}+\Gamma_{1,2}^{2}\Gamma_{1,tx}^{2}e^{-4\gamma_1 l_1}+\cdots+\Gamma_{1,2}^{M}\Gamma_{1,tx}^{M}e^{-2M\gamma_1 l_1}\right)\\
&= V_0 \mathrm{T}_{tx,1}\mathrm{T}_{1,2}e^{-\gamma_1 l_1}\frac{1-\left(\Gamma_{1,2}\Gamma_{1,tx}e^{-2\gamma_1 l_1}\right)^{M+1}}{1-\Gamma_{1,2}\Gamma_{1,tx}e^{-2\gamma_1 l_1}}\\
&= V_0 \mathrm{T}_{tx,1}\mathrm{T}_{1,2}e^{-\gamma_1 l_1}CM_1(M) \qquad (11)
\end{aligned}
$$

where $M = 0,1,2,\ldots$ is defined as the number of wave reflections in the same stripline segment, and

$$CM_i(M) = \frac{1-\left(\Gamma_{i,i+1}\Gamma_{i,i-1}e^{-2\gamma_i l_i}\right)^{M+1}}{1-\Gamma_{i,i+1}\Gamma_{i,i-1}e^{-2\gamma_i l_i}} \qquad (12)$$

Generally, due to the loss and reflections: $\left|\Gamma_{i,i+1}\Gamma_{i,i-1}e^{-2\gamma_i l_i}\right| < 1$

Therefore,

$$\lim_{M\to\infty} CM_i(M) = \frac{1}{1-\Gamma_{i,i+1}\Gamma_{i,i-1}e^{-2\gamma_i l_i}} \qquad (13)$$

and the incident wave including infinite number of reflections is:

$$
\begin{aligned}
\lim_{M\to\infty} MW_{1,2}^{0}(M) &= \lim_{M\to\infty} V_0 \mathrm{T}_{tx,1}\mathrm{T}_{1,2}e^{-\gamma_1 l_1}CM_1(M)\\
&= V_0 \mathrm{T}_{tx,1}\frac{\mathrm{T}_{1,2}e^{-\gamma_1 l_1}}{1-\Gamma_{i,i+1}\Gamma_{i,i-1}e^{-2\gamma_i l_i}} \qquad (14)
\end{aligned}
$$

The superscript 0 in $MW_{1,2}^{0}$ indicates 0^{th} orders of reflections between different segments, which will be defined more specifically later.

Similarly, the wave incident from the 2nd stripline to the 3rd stripline and the wave incident to the receiver can be calculated:

$$MW_{2,3}^{0}(M) = MW_{1,2}^{0}(M)\cdot \mathrm{T}_{2,3}e^{-\gamma_2 l_2}CM_2(M) \qquad (15)$$

$$MW_{3,rx}^{0}(M) = MW_{2,3}^{0}(M)\cdot \mathrm{T}_{3,rx}e^{-\gamma_3 l_3}CM_3(M) \qquad (16)$$

Based on (11), (12), (15) and (16), a more generalized formulation for the incident wave in a cascaded transmission line system with N segmentations can be written as:

$$MW_{A,A+1}^{0}(M) = V_0 \mathrm{T}_{tx,1} \prod_{i=1}^{A} \left[e^{-\gamma_i l_i} \cdot T_{i,i+1} \cdot CM_i(M) \right] \tag{17}$$

for $1 \leq A \leq N$.

Then, the reflections between multiple segments need to be evaluated, as shown in Figure 4.

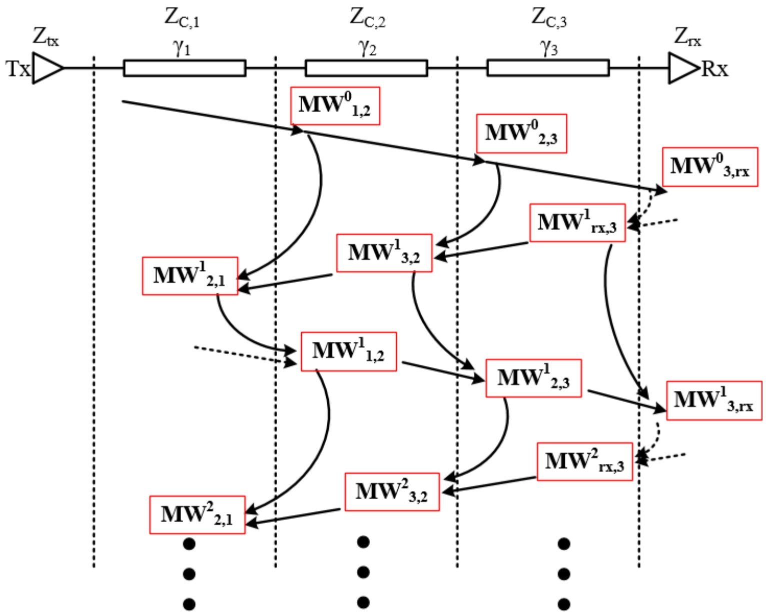

Figure 4. Wave reflections between multiple transmission line segments; all inter-section reflections.

In Figure 4, $MW_{i,j}^{M'}$ indicates the total wave incident from stripline segment i to stripline segment j, and the superscript M' is defined as the number of reflections and transmissions between multiple stripline segments.

Because there is no further discontinuity before the transmitter and after the receiver, there is no wave reflecting into the 1st segment or reflecting back at the last segment, which are marked with dashed arrows in Figure 4, and for $M' > 0$:

$$MW_{0,1}^{M'}(M) = MW_{tx,1}^{M'}(M) = 0 \tag{18}$$

$$MW_{N+1,N}^{M'}(M) = MW_{rx,N}^{M'}(M) = 0 \tag{19}$$

When $M' = 0$, the formulation has been derived as (17).

For $M' > 0$, the backward components:

$$\begin{aligned} MW_{A+1,A}^{M'}(M) = \big[&MW_{A,A+1}^{M'-1}(M) \cdot e^{-\gamma_{A+1}l_{A+1}}\Gamma_{A+1,A+2} + MW_{A+2,A+1}^{M'}(M)\big] \\ &\cdot e^{-\gamma_{A+1}l_{A+1}}\mathrm{T}_{A+1,A} CM_{A+1}(M) \end{aligned} \tag{20}$$

for $1 \leq A \leq (N-1)$.

Therefore, the insertion loss of the cascaded system can be derived as:

$$S_{21}(\omega, M, M') = \frac{1}{V_0}\sum_{k=0}^{M'} MW_{N,N+1}^{k}(\omega, M) \tag{21}$$

Based on the definition of the S-parameters, all wave components received at the receiver needs to be considered. So, the actual transmission coefficient of the system is

$$S_{21}(\omega) = \frac{1}{V_0}\lim_{M,M'\to\infty}\sum_{k=0}^{M'} MW_{N,N+1}^{k}(\omega, M) \tag{22}$$

2.3. S-PARAMETER NETWORKS IN THE CASCADED CHANNEL

In many practical designs, there are some parts of the channel that are not ideal transmission-line structures, like the via transition structures. For these non-ideal transmission-line structures, S-parameter networks from full-wave simulations or measurements are usually used in channel analysis. Thus, the reflections and propagations with cascaded S-parameter network are analyzed and the formulations are extended to handle the cascaded channel with non-ideal transmission-line structures.

As shown in Figure 5, at the ports of S-parameter network, there are 2 kinds of reflection mechanisms: 1) the reflections due to the impedance mismatch between the external cascaded channel and the S-parameter reference impedance ($Z_C \neq Z_{ref}$); and 2) the reflections inside the S-parameter network (return loss S_{ii}).

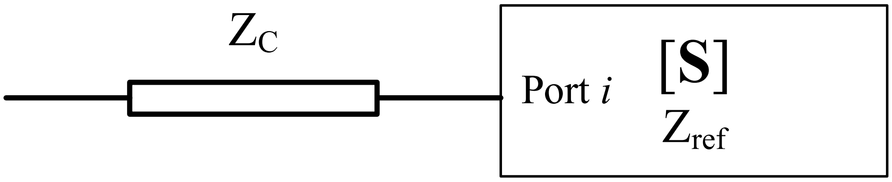

Figure 5. An S-parameter network (with reference impedance Z_{ref}) cascaded to a transmission-line at Port i.

The S-parameter reference impedance Z_{ref} is the system impedance of the network. For example, the common system impedance for a VNA is 50 Ohms.

To use the similar method to analyze the wave reflections and propagations with S-parameter networks, special treatments are needed, and 2 different approaches are proposed.

2.3.1. Method 1: Adding Pseudo Segments. By adding a pseudo segment in the middle between the external channel and the S-parameter network port, the reflections due to 2 different reflection mechanisms can be separated, and the previous method to derive the closed-form formulations can be applied. The length of the pseudo segment should be 0, and the characteristic impedance of the pseudo segment should be the reference impedance of the S-parameter. The reflections at the S-parameter network with the additional pseudo segment are shown in Figure 6.

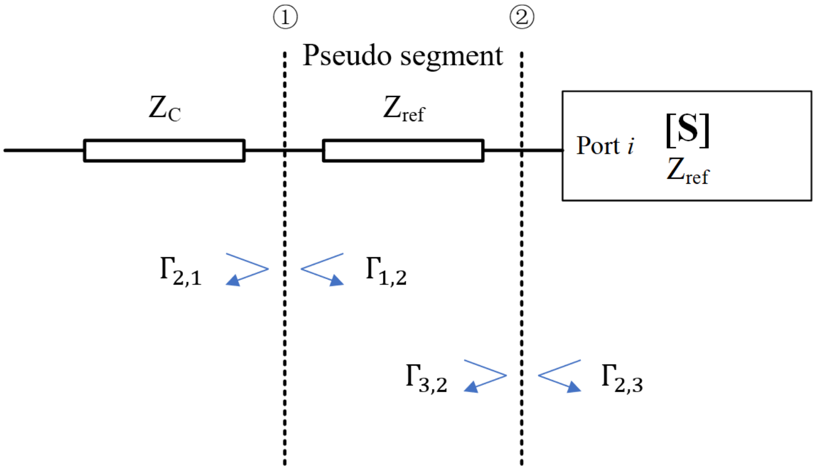

Figure 6. Adding a pseudo segment at ports of S-parameter network to separate 2 kinds of reflections.

Since the length of the pseudo segment is $l_{pseudo} = 0$ and there is no loss and no phase delay for the wave propagation on the pseudo segment:

$$e^{-\gamma l_{pseudo}} = 1 \tag{23}$$

At the interface #1, there are only the reflections due to the impedance mismatch $Z_C \neq Z_{ref}$, and

$$\Gamma_{2,1} = \frac{Z_{ref} - Z_C}{Z_{ref} + Z_C} \tag{24}$$

$$\Gamma_{1,2} = \frac{Z_C - Z_{ref}}{Z_C + Z_{ref}} \tag{25}$$

At the interface #2, there are only the reflections from inside of the S-parameter network S_{ii}, and

$$\Gamma_{3,2} = S_{ii} \tag{26}$$

$$\Gamma_{2,3} = 0 \tag{27}$$

Based on this method, an example of all the wave propagations and reflections in a cascaded channel with S-parameter network is shown in Figure 7.

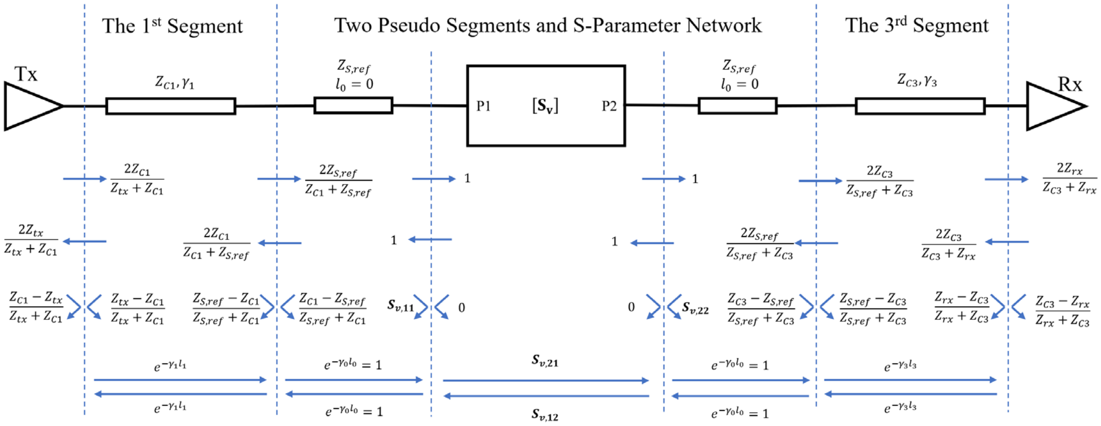

Figure 7. Method 1: Adding Pseudo Segments - wave propagations and reflections in a cascaded channel with S-parameter network.

After adding the pseudo segments at the ports of the cascaded S-parameter network, the same method in the previous section can be used to derive the closed-form formulation of this cascaded channel.

2.3.2. Method 2: S-Parameter Re-Normalization. Rather than adding additional pseudo segments at the ports of S-parameter networks, another possible approach is to remove the reflections due to the impedance mismatch by S-parameter re-normalization. When $Z_C = Z_{ref}$, there will only be the reflections due to the return loss of the S-parameter network.

As mentioned in the previous section, the characteristic impedance of the external cascaded channel can be frequency-dependent and complex, which is not common for S-parameter reference impedance. In addition, the characteristic impedances of the external channels can be different at different S-parameter ports. Therefore, the S-parameter re-normalization needs to be done at each single frequency, and the re-normalized S-parameter may have different reference impedances at different ports.

In [16], the formulation for S-parameter re-normalization is introduced:

$$[S_{new}] = [P]^{-1}([S_{old}] - [\gamma])([I] - [\gamma][S_{old}])^{-1}[P] \tag{28}$$

where $[S_{new}]$ and $[S_{old}]$ are $n \times n$ S-parameter matrices after and before the re-normalization; $[P]$ and $[\gamma]$ are diagonal matrices. Let $Z_{new,ii}$ and $Z_{old,ii}$ be the new and old reference impedances at port i:

$$\gamma_{ii} = \frac{Z_{new,ii} - Z_{old,ii}}{Z_{new,ii} + Z_{old,ii}} \tag{29}$$

$$P_{ii} = \sqrt{\frac{Re(Z_{old,ii})}{Re(Z_{new,ii})}} \cdot \left|\frac{Z_{new,ii}}{Z_{old,ii}}\right| \cdot \frac{2Z_{old,ii}}{Z_{old,ii} + Z_{new,ii}} \tag{30}$$

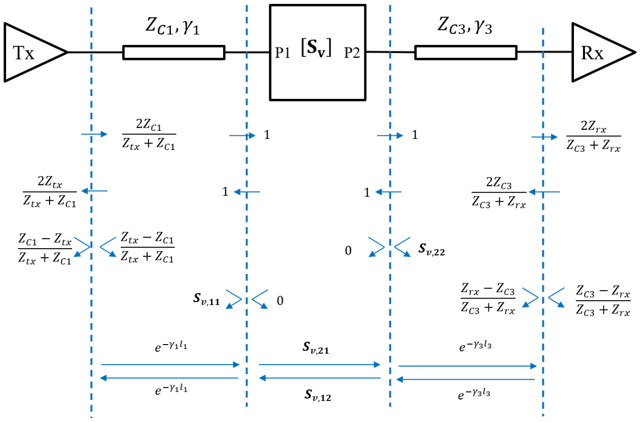

Figure 8. Method 2: S-Parameter Re-Normalization - wave propagations and reflections in a cascaded channel with S-parameter network.

After the S-parameter re-normalization, an example of all the wave propagations and reflections in a cascaded channel with S-parameter network is shown in Figure 8.

Also, the same method in the previous section can be used to derive the closed-form formulation of this cascaded channel. Both methods proposed above are equivalent, applicable to different scenarios are shown below.

3. VALIDATION OF THE FORMULATIONS

As shown in Figure 9, an example of a differential channel with the S-parameter of a via transition structure from the full-wave simulation is designed to validate the correctness of the derived formulations and the handling of cascaded S-parameter networks.

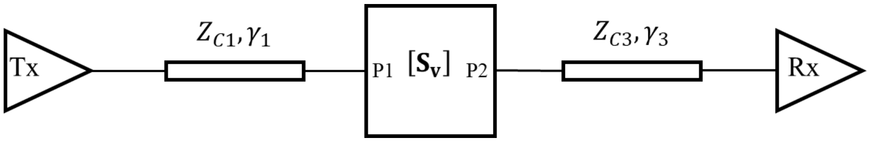

Figure 9. An example of a differential channel with S-parameter of a via transition structure with 50 Ohms reference impedance.

The odd-mode impedances of the transmitter and the receiver are $Z_{tx} = Z_{rx} = 50\ \Omega$. The 1st and the 3rd segments are symmetrical differential striplines with the same cross-sectional geometries, and the related parameters can be found in Table 1.

The S-parameter network is from a full-wave simulation on a via transition structure. The via structure is shown in Figure 10. The geometry information of the via structure can be found in Table 2. The frequency range of the full-wave simulation is from 10 MHz to 100 GHz.

Table 1. Parameters of the Channel

Parameters	Values
Total dielectric thickness b	35.6 mils
Trace width W	16 mils
Trace spacing s	32 mils
Trace thickness t	1.38 mils
Length of trace l_1 and l_3	400 mils
Resistance of metal ρ	$1.764 \times 10^{-8}\ \Omega m$
ε_r' @ 1 GHz	3.7
$\tan\delta$ @ 1 GHz	0.02
Djordjevic model f_L	1 kHz
Djordjevic model f_H	1000 THz
G_p	1.5
ε_0	8.854×10^{-12} F/m
μ_0	$4\pi \times 10^{-7}$ H/m

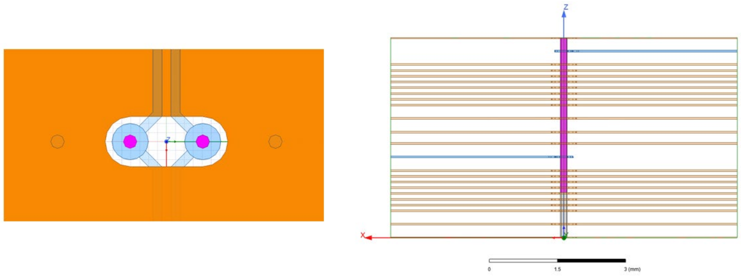

(a) (b)

Figure 10. The via structures in the full-wave simulation (a) top view; and (b) the side view.

Table 2. Parameters of the Via

Parameters	**Values**
Via diameter	6 mils
Via spacing	32 mils
Anti-pad diameter	22 mils
Pad diameter	16 mils
Length of active via	91.8 mils
Length of via stub	30 mils

Let $M \rightarrow \infty$ and $M' = 20$ in the calculation of S_{21} using the derived analytical formulations to ensure that enough number of wave reflections have been included in the calculation, and the results are shown in Figure 11.

In Figure 11, we have the following denotations on the methods:

- Method 1 is the pseudo segment method. Pseudo segments are added at the ports of S-parameter networks, as shown in Figure 7.
- Method 2 is the re-normalization method. S-parameters of the middle segment have been re-normalized to the external channel's characteristic impedances $Z_{C,1}$ and $Z_{C,3}$ at port 1 and port 2, respectively (Figure 8).
- Method 3 is the reference result, and it is obtained from ADS simulations.

All these results have good correlations, indicating that the proposed methods have good accuracy, and the cascaded S-parameter network is properly treated.

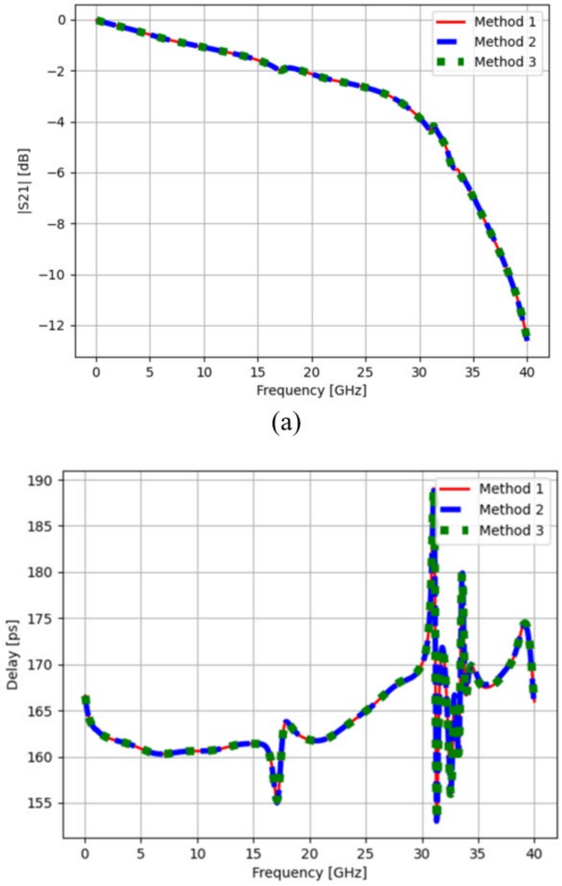

(a)

(b)

Figure 11. The comparisons on (a) $|S_{21}|$ and (b) group delay from 3 different methods.

4. APPLICATIONS TO CHANNEL OPTIMIZATIONS

When evaluating a high-speed signal channel, eye opening in the eye-diagram is a common criterion, and the inter-symbol interference (ISI) has negative impacts on the eye opening. ISI can be identified clearly in the single-bit response (SBR) of the channel. Thus, it is possible to optimize the channel based on the SBR. The reflections in a cascaded channel generate additional ripples in the SBR after the main peak and are one of the important contributors to the ISI. Smaller ripples due to reflections in SBR means larger eye opening. Also, if DFEs are going to be added at the receiver to improve the signal quality, less voltage compensation and less power consumption will be needed.

Table 3. Parameters of the Channel in Figure 12.

Parameters	**Values**
Total dielectric thickness b	23.4 mils
Trace width W	4 mils
Trace spacing s	4 mils
Trace thickness t	1.38 mils
Resistance of metal ρ	$1.764 \times 10^{-8}\ \Omega m$
ε_r' @ 1 GHz	3.7
$\tan\delta$ @ 1 GHz	0.02
Djordjevic model f_L	1 kHz
Djordjevic model f_H	1000 THz

Since the proposed method for evaluating cascaded channels is based on analyzing the wave propagations and reflections individually, the generation of each individual ripples in the SBR can be backtracked. The steps of the proposed channel optimization method are shown below. A cascaded high-speed differential channel with 3 stripline segments and 2 via transition structures is used as the example and the schematic of the cascaded channel is shown in Figure 12.

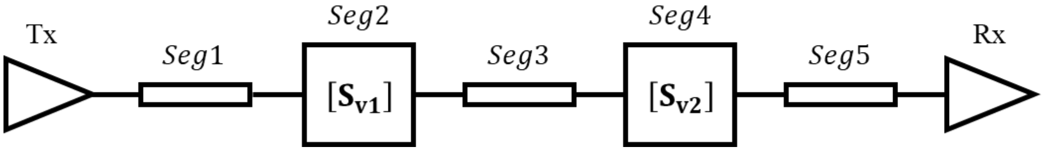

Figure 12. A cascaded high-speed differential channel with 3 stripline segments and 2 via transition structures.

The cross-sectional geometry of the three striplines are the same and the parameters are shown in Table 3. l_1, l_3 and l_5 are the lengths of the 3 stripline segments and the values are 100 mils, 300 mils and 600 mils, respectively. The odd-mode transmitter and receiver impedances are $Z_{tx} = Z_{rx} = 45\ \Omega$, and the odd-mode characteristic impedance of the 3 striplines are also around 45 Ohms. The steps of the optimization process are given below:

Step 1: Identify the critical ripples to optimize in SBR

Use the method proposed in the previous sections to calculate the S_{21} of the cascaded channel. Then, the SBR of the system can be calculated, which is shown in Figure 13. The data rate of the signal is 56 Gbps. To avoid unwanted behavior in the SBR due to bandwidth limitation of the S-parameter, a Gaussian filter with cut-off frequency at 84 GHz $(1.5 \times \text{data rate})$ is added on the input single-bit waveform.

Step 2: Backtrack the propagation path and reflections related to the critical ripples

In the SBR of the cascaded channel shown in Figure 13, there is a group of ripples at around 400 ps (marked with red dashed rectangle) with relatively larger magnitudes, and these are the most critical ripples contributing to the total ISI.

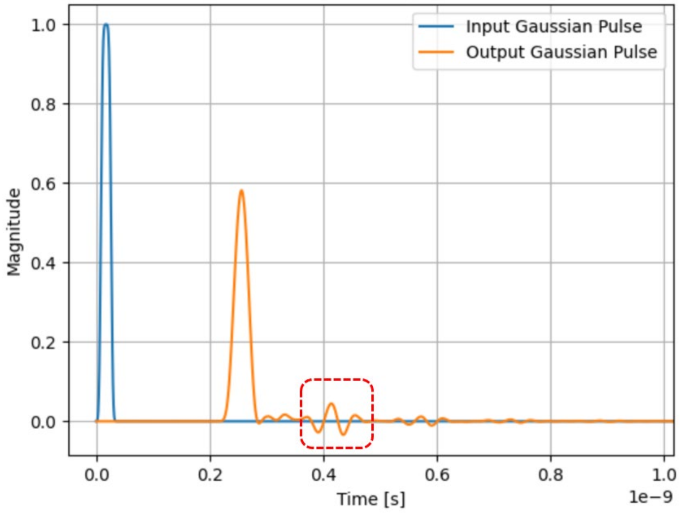

Figure 13. Single-Bit responose of the cascaded channel shown in Figure 12, and the critical ripples after the main pulse.

As discussed in the previous sections, all the ripples in the SBR with different propagation paths and reflections can be analyzed individually. The steps to sort out all the ripples are summarized below:

1) Estimate the magnitudes of the transmission coefficients and reflection coefficients between all segments in the cascaded channel, and the propagation constant of each segment. These values are going to be used to estimate the magnitudes of the transmitted and reflected waves at each interface of cascading. The estimations can be done at a single chosen frequency using (7) ~ (10).
2) From the incident wave sent from the transmitter, calculate the estimated magnitudes of all possible transmitted waves and reflected waves at each interface between segments. This calculation on the wave magnitude estimation stops when the estimated wave magnitude becomes less than a pre-defined threshold value, e.g., 0.01. If the wave magnitude is less than the threshold value, it means that the wave magnitude is

too small, and the wave is negligible in the total SBR waveforms. After this step, all the wave components in the cascaded channel with certain magnitudes are sorted out and their propagation paths in the cascaded channel are recorded.

3) Find the wave components at the receiver of the channel from the results of the previous step. Based on their propagation paths in the cascaded channel, the frequency-domain transfer function of each individual ripple can be calculated using the frequency-dependent coefficients, not the estimated values. Then, the time-domain waveforms of each individual ripple can be calculated using iFFT.

The first a few ripples in the original SBR and their propagation paths are shown in Figure 14, where the magnitudes of ripples are diminished away from the main pulse.

The formulation for the main pulse is

$$V_{main} = V_{in} \cdot e^{-\gamma_1 l_1} \cdot S_{v1,21} \cdot e^{-\gamma_3 l_3} \cdot S_{v2,21} \cdot e^{-\gamma_5 l_5} \cdot \mathrm{T}_{tx,1}\mathrm{T}_{1,2}\mathrm{T}_{2,3}\mathrm{T}_{3,4}\mathrm{T}_{4,5}\mathrm{T}_{5,rx} \tag{31}$$

It is easy to identify that the critical ripples in the SBR (Figure 13) is related with the propagation path #2 in Figure 14(a), and the corresponding formulation is

$$V_{ripple} = V_{in} \cdot e^{-\gamma_1 l_1} \cdot S_{v1,21} \cdot e^{-\gamma_3 l_3} \cdot S_{v2,21} \cdot e^{-\gamma_5 l_5} \cdot \mathrm{T}_{tx,1}\mathrm{T}_{1,2}\mathrm{T}_{2,3}\mathrm{T}_{3,4}\mathrm{T}_{4,5}\mathrm{T}_{5,rx} \cdot \boldsymbol{e^{-2\gamma_3 l_3}\Gamma_{2,3}\Gamma_{4,3}} \tag{32}$$

Based on the previous assumptions, the 3 striplines have the same cross-sectional geometries, so $\gamma_1 = \gamma_3 = \gamma_5$. If the total length of the PCB stripline segments are kept the same, the magnitude of these ripples will be affected by the bolded term $e^{-2\gamma_3 l_3}\Gamma_{2,3}\Gamma_{4,3}$ in (32). Therefore, to mitigate the ripple magnitude, the possible approaches are: 1) increase the length of the middle segment l_3 and 2) reduce the reflections between the middle stripline and the via structures $\Gamma_{2,3}$ and $\Gamma_{4,3}$.

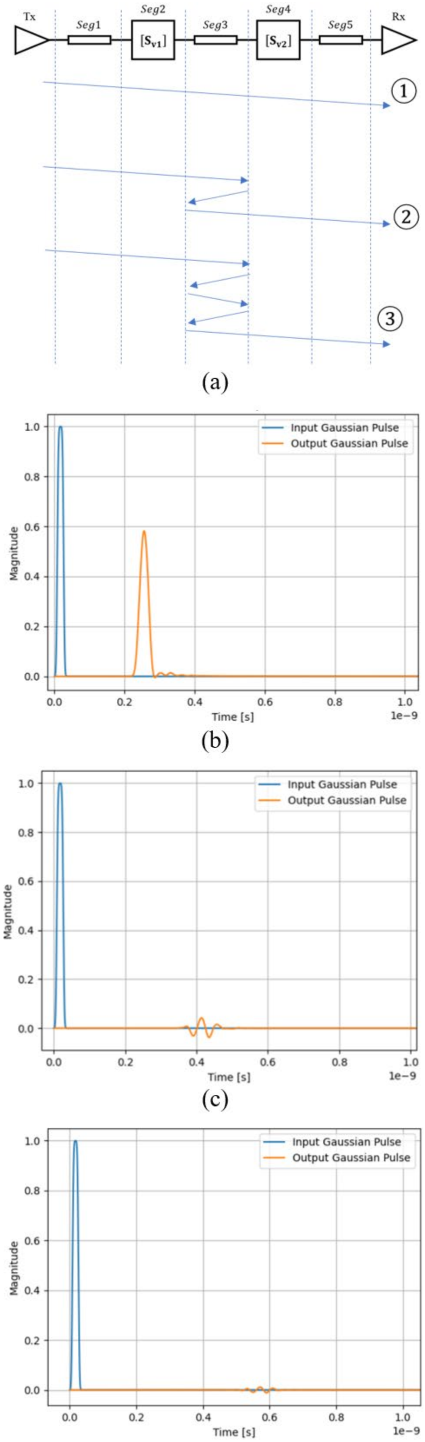

(a)

(b)

(c)

(d)

Figure 14. (a) The first 3 ripples propagation paths in the cascaded channel; (b) the time-domain response of the ripple with path # 1; (c) the time-domain response of the ripple with path # 2; (d) the time-domain response of the ripple with path # 3.

Step 3: Optimize the channel based on the previous analysis

1) Tuning the distance between the 2 vias (l_3)

Optimizing the via structures is necessary to reducing the reflections when designing high-speed channels, but there are always some reflections after the via optimizations. Also, the most optimized via structures may not be able to be implemented in practical designs due to limitations on spacing or manufacturing.

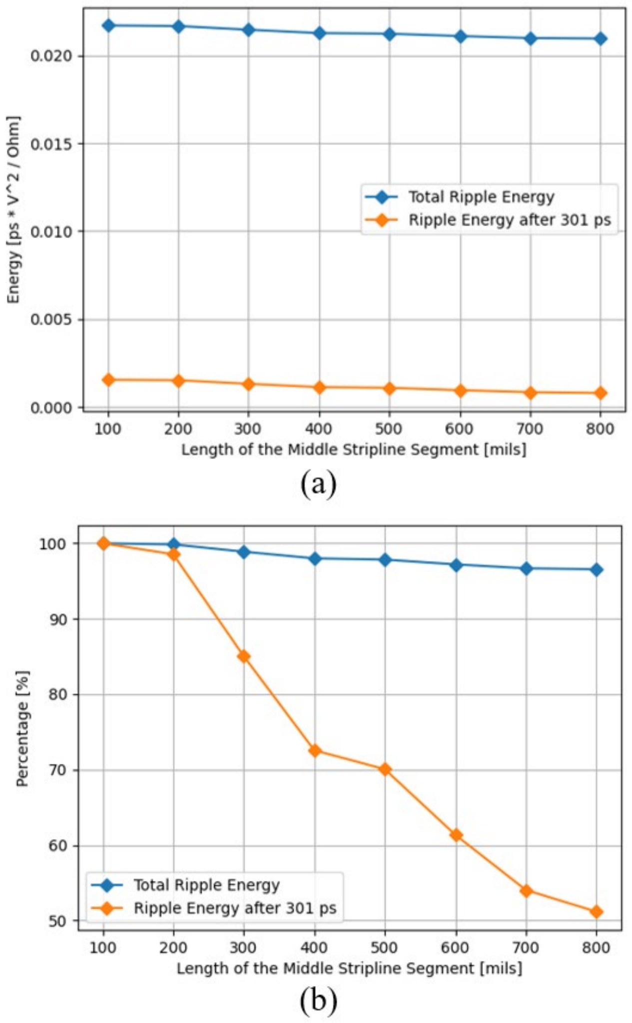

Figure 15. The change of ripples in the SBR with different distances between the 2 vias (a) ripple energy; and (b) percentage of ripples energy reduction.

However, the analysis in the previous section indicates that it is possible to mitigate the ripple magnitudes by tuning the locations of vias in the cascaded channel. While keeping the total length of the channel and the length of the 1st PCB stripline segment to be 1 inch and 100 mils, respectively, the length of the middle stripline segment is swept from 100 mils to 800 mils, and the changes of ripples are shown in Figure 15.

The ripple energy in Figure 15 is calculated by:

$$E_{ripple} = \int_{t_0}^{\infty} \frac{V^2 \cdot dt}{R} \tag{33}$$

where $R = 45\ \Omega$ is the system's impedance of the cascaded channel, and the unit of the calculated ripple energy from (33) is $V^2 \cdot s/\Omega$, which is equivalent to Joule. This ripple energy is used in both Figure 15(a) and Table 4 to evaluate the ripple behaviors in the time-domain response.

Table 4. Ripples and Eye Opening with Different W_3 (Tuning $\Gamma_{2,3}$ and $\Gamma_{4,3}$)

$\boldsymbol{W_3}$	**2 mils**	**4 mils**	**6 mils**
Estimated $\Gamma_{2,3}$ and $\Gamma_{4,3}$	0.454	0.493	0.503
Ripple energy after the main pulse [pJ]	0.0010167	0.0011765	0.001275
Percentage of ripple energy after the main pulse	86.4%	100 %	108.4 %
Eye height [V]	0.061	0.098	0.089
Eye width [ps]	8.34	9.37	9.84
Eye area [V · ps]	0.50874	0.91826	0.87576

In Figure 15, the calculation of total ripple energy starts the energy integration at half UI after the peak of the main pulse, and the main pulse has not ended yet. Thus, a part of the main pulse is also included in the ripple evaluation. To completely focus on the change of the critical ripples happening around 400 ps, the ripple energy calculation starting from 301 ps is also included in Figure 15. The main pulse has ended before 301 ps and the energy integration after that is dominant by the critical ripples.

The change of ripples is consistent with the analysis in the previous section: when the length of the middle stripline segment increases, the magnitude and the energy of the critical ripples reduce significantly.

The eye openings of the original channel (300-mil distance between the 2 vias) and the optimized channel (800-mil distance between the 2 vias) are also compared, as shown in Figure 16.

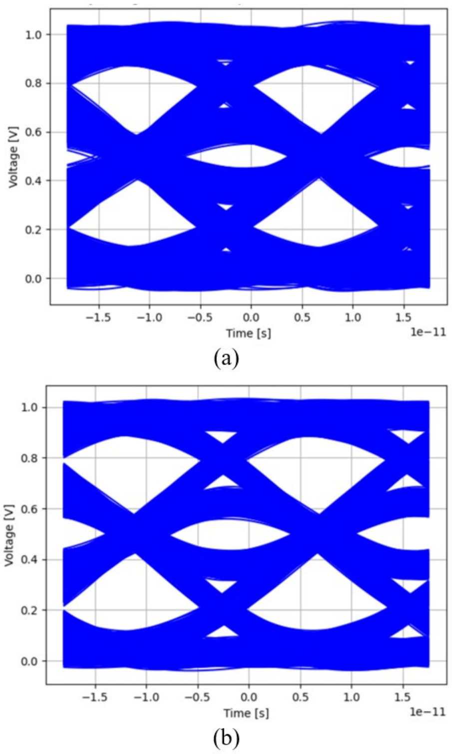

(a)

(b)

Figure 16. The eye diagram of the 1-inch channel (a) before optimization; and (b) after optimization.

The eye height and the eye width of the original channel are 0.098 V and 10.38 ps, respectively; and the eye height and the eye width of the optimized channel are 0.1255 V and 12.06 ps, respectively. Therefore, after changing the distance between the 2 vias from 300 mils to 800 mils, the area of the eye opening becomes 48.8 % larger.

2) Tuning the reflections $\Gamma_{2,3}$ and $\Gamma_{4,3}$

The reflections $\Gamma_{2,3}$ and $\Gamma_{4,3}$ can be tuned by changing the characteristic impedance, or the width, of the middle segment *Seg 3* in Figure 12. The differences comparing to the previous optimization method is that the values of other parameters ($T_{2,3}$, $T_{3,4}$ and γ_3) will change when tuning these reflection coefficients $\Gamma_{2,3}$ and $\Gamma_{4,3}$. These parameters exist in both (31) and (32), which means that the behavior of the main pulse will also be impacted when tuning $\Gamma_{2,3}$ and $\Gamma_{4,3}$.

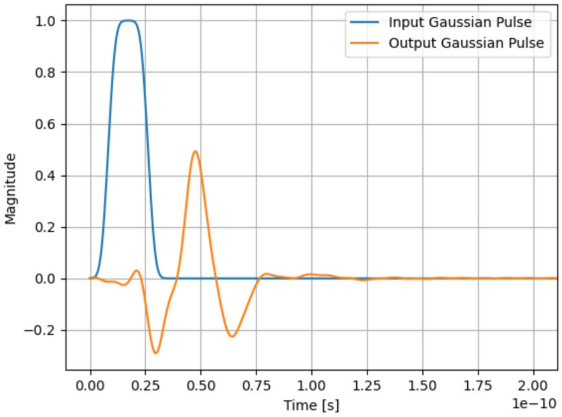

Figure 17. Estimating the reflection coefficient at the S-parameter port based on time-domain response.

In addition, the reflection at the S-parameter network ports could not be calculated by the ratio of characteristic impedances, as revealed by (10). Since the behavior of ripples in time-domain responses is discussed and analyzed, the estimated reflection coefficient at the S-parameter port is defined as the ratio of the peak voltage level of the input pulse and the reflected waveform at the port, as shown in Figure 17.

In the original design, the trace width of *Seg 3* (W_3) is 4 mils, and the estimated reflection coefficient is 0.493. Two more cases with $W_3 = 2\ mils$ and $W_3 = 6\ mils$ are evaluated, and the results are summarized in Table 4.

As shown in Table 4, when the trace width of *Seg 3* (W_3) decreases from 4 mils to 2 mils, the estimated reflection level at the S-parameter ports decreases, and the ripple energy becomes 86.4 % compared to the original design; when the trace width of *Seg 3* (W_3) increases from 4 mils to 6 mils, the estimated reflection level at the S-parameter ports increases, and the ripple energy becomes 108.4 % compared to the original design. The change of ripple behaviors is consistent with the expectations. However, when $W_3 = 2\ mils$, the ripple is the minimum in all the 3 cases, but the eye opening is also the smallest. The reason is that the transmission coefficients and the propagation constant of Seg 3 become different when tuning the trace width, and the behavior of the main pulse is also impacted. The 2-mil trace has much larger loss compared to the 4-mil trace, and the larger loss in the channel introduces a negative impact on the eye opening at the receiver side.

In this section, the channel optimizations based on the derived closed-form formulations are demonstrated using a few examples. After identifying the propagation paths and the reflections related to the critical ripples in the time-domain response by backtracking, the effective approaches to mitigate the ripples and enlarge eye openings can be determined. The effectiveness of the optimizations is validated using both single-bit response and eye diagrams. In the optimization example (Figure 12), tuning the distance between the 2 vias is the more effective method to mitigate the magnitudes of ripples and improve the eye opening. The eye height or the eye opening in the eye diagram is more directly related to the performance of a high-speed channel compared to the ripples in the channel's SBR. If the magnitude of the main pulse in the SBR remains the same during the tuning, like tuning the distance between the 2 vias in the previous example, reducing the magnitudes of ripples in the SBR can help improve the eye opening. If the channel tuning changes the response of the main pulse in the SBR, more attention should be paid to the tuning and the balance between larger main pulse and smaller ripples in the SBR should be determined to achieve the optimal response of the cascade channel.

5. CONCLUSION

In this paper, novel formulations of multi-reflections in cascaded channels are proposed. The applications to optimize high-speed channels using the outlined formulations are also discussed. The formulations are derived by evaluating all wave reflections and propagations separately. Compared to the formulations published in the previous studies [13], where only the single-ended systems were investigated, we validate the correctness and accuracy of the formulation in differential cascaded systems with S-parameter networks.

One of the most important advantages of the proposed novel formulations in this study is that ripples in the single-bit response can be backtracked according to our newly derived reflection formulations combining both frequency-domain and time-domain responses: the propagation paths and the reflections of each individual ripple in the single-bit response can be identified, and the corresponding transmission function can be determined. After identifying critical ripples in the single-bit response that need to be optimized, the channel parameters that impact the ripple behavior can be located, which would provide more precise guidance for designers to optimize the cascaded channel.

REFERENCES

[1] H. Wu, M. Shimanouchi and M. PengLi, "Effective Link Equalizations for Serial Links at 112 Gbps and Beyond," *2018 IEEE 27th Conference on Electrical Performance of Electronic Packaging and Systems (EPEPS)*, San Jose, CA, USA, 2018, pp. 25-27.

[2] B. Chen *et al.*, "Differential integrated crosstalk noise (ICN) reduction among multiple differential BGA and Via pairs by using design of experiments (DoE) method," *2017 IEEE International Symposium on Electromagnetic Compatibility & Signal/Power Integrity (EMCSI)*, Washington, DC, USA, 2017, pp. 112-117.

[3] B. Chen, S. Pan, J. Wang, S. Yong, M. Ouyang and J. Fan, "Differential Crosstalk Mitigation in the Pin Field Area of SerDes Channel With Trace Routing Guidance," in *IEEE Transactions on Electromagnetic Compatibility*, vol. 61, no. 4, pp. 1385-1394, Aug. 2019.

[4] S. Yong, K. Cai, B. Sen, J. Fan, V. Khilkevich and C. Sui, "A Comprehensive and Practical Way to Look at Crosstalk for Transmission Lines with Mismatched Terminals," *2018 IEEE Symposium on Electromagnetic Compatibility, Signal Integrity and Power Integrity (EMC, SI & PI)*, Long Beach, CA, USA, 2018, pp. 538-543.

[5] C. Johansson and T. Månefjord, "Analysis of a high-speed PCB design," *2017 IEEE Nordic Circuits and Systems Conference (NORCAS): NORCHIP and International Symposium of System-on-Chip (SoC)*, Linköping, Sweden, 2017, pp. 1-4.

[6] S. Yong *et al.*, "Prepreg and Core Dielectric Permittivity (ϵ_r) Extraction for Fabricated Striplines' Far-End Crosstalk Modeling," in *IEEE Transactions on Electromagnetic Compatibility*.

[7] D. M. Pozar, Microwave Engineering, 4th ed. New York, NY, USA: Wiley, 2012.

[8] J. Ajanovic, "PCI express 3.0 overview," *2009 IEEE Hot Chips 21 Symposium (HCS)*, Stanford, CA, USA, 2009, pp. 1-61.

[9] Y. -. E. Yang and Qizheng Gu, "Time-Domain Perturbational Analysis of Nonuniformly Coupled Transmission Lines," in *IEEE Transactions on Microwave Theory and Techniques*, vol. 33, no. 11, pp. 1120-1130, Nov. 1985.

[10] R. J. Allred, B. Katz and C. Furse, "Ripple analysis: Identify and quantify reflective interference through ISI decomposition," *2016 IEEE 20th Workshop on Signal and Power Integrity (SPI)*, Turin, Italy, 2016, pp. 1-4.

[11] H. Erkens and H. Heuermann, "Mixed-Mode Chain Scattering Parameters: Theory and Verification," in *IEEE Transactions on Microwave Theory and Techniques*, vol. 55, no. 8, pp. 1704-1708, Aug. 2007.

[12] L. Yang and G. Yu, "A New Method to Calculate Cascaded S-Parameters," *2018 IEEE 27th Conference on Electrical Performance of Electronic Packaging and Systems (EPEPS)*, San Jose, CA, USA, 2018, pp. 71-73.

[13] M. Ouyang *et al.*, "An Investigation on Multiple Reflections and Group Delay Behavior in High-Speed System Designs," *2021 IEEE International Joint EMC/SI/PI and EMC Europe Symposium*, Raleigh, NC, USA, 2021, pp. 423-428.

[14] G. Yin, X. Cai, D. Secker, M. Ortiz, J. Cline and A. Vaidyanath, "Impedance Perturbation Theory for Coupled Uniform Transmission Lines," in *IEEE Transactions on Electromagnetic Compatibility*, vol. 57, no. 2, pp. 299-308, April 2015.

[15] A. R. Djordjevic, R. M. Biljie, V. D. Likar-Smiljanic and T. K. Sarkar, "Wideband frequency-domain characterization of FR-4 and time-domain causality," in *IEEE Transactions on Electromagnetic Compatibility*, vol. 43, no. 4, pp. 662-667, Nov. 2001.

[16] D. Woods, “Multiport-network analysis by matrix renormalization employing voltage-wave S-parameters with complex normalization,” *Proc. Inst. Elec. Eng.*, vol. 124, pp. 198-204, Mar. 1977.

II. IMPROVEMENT OF CONVERGENCE CHARACTERISTICS IN THE GENERALIZED MULTICONDUCTOR TRANSMISSION-LINE METHOD NEAR RESONANT FREQUENCIES

ABSTRACT

This paper presents an approach to improve the convergence characteristics of the generalized multiconductor transmission-line (GMTL) method near the resonant frequencies of the system. In the GMTL method, the current distributions on cable harness are solved iteratively using the perturbation method. Therefore, the correctness of the solution can only be guaranteed when the iterations in the perturbation method are converged, but this requirement on convergence usually fails near the resonant frequencies of the cable harness system. Near the resonant frequencies, the cable harness system tends to be more radiative, and the cable currents associated with the radiation becomes more dominant. These radiative currents are not considered in the classic transmission-line theory and cause the failure of convergence. To improve the convergence characteristics of the perturbation method, additional resistances representing the radiation loss in the transmission-line system are added in the GMTL method, and the modified GMTL method with additional resistances show good convergence characteristics in frequency bands away from the resonant frequencies and near the resonant frequencies.

Keywords: Cable harness, Convergence, Multiconductor transmission-line, Perturbation method, Resonance.

1. INTRODUCTION

Cable harnesses usually contain a large number of wires and are widely used in modern vehicles to provide power to electric systems that are located at different locations throughout the vehicle as well as to establish signal channels for data communications between these systems [1]. The characteristics of the EM radiation resulting from the currents on cable harnesses in the whole vehicle system need to be evaluated carefully to avoid potential EM interference problems.

Because of the complexity of the geometry, modeling and analyzing cable harnesses using full-wave methods can be time-consuming and computational resource-intensive [2]. Therefore, the hybrid MTL method was proposed to cut down the computational effort. In the hybrid MTL method, the cable harnesses are segmented, and each segment is modeled using the lumped circuit components calculated using the transmission-line theory. Then, the cable harness system can be solved in a circuit solver, which is much faster than the full-wave method [3, 4].

Although the hybrid MTL method can solve the cable harness system efficiently, it has been reported that the accuracy of the solution is limited when 1) the length of each segment is not short enough to be an electrical small structure; 2) the separations between wires and nearby ground planes are large; and 3) the geometries of the harnesses and nearby planes are not homogeneous, i.e., there are slots in the nearby planes or the distance between wires and planes keeps changing [2, 5]. The GMTL method was proposed to overcome certain limitations. In the GMTL method, correction terms on the current and potential calculations are added and the perturbation method is implemented to solve the currents and potential distributions along the cable harnesses with correction terms iteratively [6, 7]. The calculation results from the GMTL method have better consistence to the full-wave solutions compared to the original hybrid MTL results, but the iterative calculations in the GMTL method may not converge near the resonant frequencies of the cable harness system [5, 6]. Based on the theory of the perturbation method, when the calculation is not converged, the calculation will not give correct results.

In this paper, the failure of convergence in the GMTL method near resonant frequencies is analyzed to explain why the perturbation method in GMTL will fail near resonant frequencies of the cable harness system. Then, the solution on this convergence issue is proposed. By considering the radiation loss of the cable harness system using additional resistances in the transmission-line model, the iterative calculations of the perturbation method can remain converged in frequency bands near resonant frequencies and calculation results consistent with the full-wave solutions can be obtained.

The organization of this paper is briefly summarized here. In Section II, the GMTL method is briefly reviewed, and the convergence issue in the perturbation method near resonant frequencies of the cable harness system is analyzed. In Section III, the resistances representing the radiation loss in MTL systems are introduced and the modified formulations of the GMTL method with the additional resistances are presented. In Section IV, the improvement on the convergence characteristics is shown using numerical examples and the results are discussed. In Section V, discussions and conclusions of this paper are given.

2. THE GENERALIZED MTL METHOD

Solving a cable harness system iteratively using the generalized MTL method was proposed in [6] and the method is briefly reviewed in this section. Then, the requirements to ensure the convergence of the iterative calculations in the GMTL method are analyzed and the explanation on the convergence issue near resonant frequencies of a cable harness system is given.

2.1. REVIEW ON THE GMTL METHOD

The governing equations of the GMTL method are shown below:

$$\begin{cases} \frac{d}{dl}\overline{\phi} + j\omega\overline{\overline{L}}\,\bar{i} = \overline{E}^{inc} + j\omega\overline{D}_1\left\{\bar{i}\right\} \\ \frac{d}{dl}\bar{i} + j\omega\overline{\overline{C}}\,\overline{\phi} = \overline{D}_2\left\{\bar{i}\right\} \end{cases} \tag{1}$$

where $\overline{\phi}$, $\bar{i}$ and $\overline{E}^{inc}$ are the vectors of the electrical potential, the current and the incident electrical field on the wires in the MTL system, respectively.

Compared to the original MTL equations, there are two more correction terms in (1):

$$\overline{D}_1\left\{\bar{i}\right\} = \overline{\overline{L}}\,\bar{i} - \overline{A} \tag{2}$$

and

$$\overline{D}_2\left\{\bar{i}\right\} = \frac{d}{dl}\bar{i} - \overline{\overline{C}}\,\overline{P} \tag{3}$$

At the observation location $\vec{r}$, $A(\vec{r})$ and $\bar{P}(\vec{r})$ can be calculated by

$$A\left(\vec{r}\right)=\mu\int_{l}i(\vec{r}')g(\vec{r},\vec{r}')d\vec{r}' \tag{4}$$

$$\bar{P}(\vec{r})=\frac{1}{\varepsilon}\int_{l}\frac{d}{dl'}i(\vec{r}')g(\vec{r},\vec{r}')d\vec{r}' \tag{5}$$

It can be noticed that the correction terms $\overline{D}_1\left\{\bar{i}\right\}$ and $\overline{D}_2\left\{\bar{i}\right\}$ in (1) compensate the differences between the classic transmission-line modeling and the full-wave mixed-potential integral equations (MPIE). Also, the left-hand side of (1) keeps the same format compared to the original MTL equations.

Then, the current and potential distributions along the MTL system can be solved through the perturbation method, where the solutions are calculated iteratively:

For $n=0$:

$$\begin{cases}\dfrac{d}{dl}\bar{\phi}_{(n)}+j\omega\overline{\overline{L}}\,\bar{i}_{(n)}=\overline{E}^{inc}\\ \dfrac{d}{dl}\bar{i}_{(n)}+j\omega\overline{\overline{C}}\,\bar{\phi}_{(n)}=\bar{0}\end{cases} \tag{6}$$

For $n\geqslant1$:

$$\begin{cases}\dfrac{d}{dl}\bar{\phi}_{(n)}+j\omega\overline{\overline{L}}\,\bar{i}_{(n)}=j\omega\overline{D}_1\left\{\bar{i}_{(n-1)}\right\}\\ \dfrac{d}{dl}\bar{i}_{(n)}+j\omega\overline{\overline{C}}\,\bar{\phi}_{(n)}=\overline{D}_2\left\{\bar{i}_{(n-1)}\right\}\end{cases} \tag{7}$$

And the final solution of (1) from the perturbation method can be written as:

$$\begin{cases}\bar{\phi}=\displaystyle\sum_{n=0}^{\infty}\bar{\phi}_{(n)}\\ \bar{i}=\displaystyle\sum_{n=0}^{\infty}\bar{i}_{(n)}\end{cases} \tag{8}$$

2.2. THE CONVERGENCE REQUIREMENT IN THE GMTL METHOD

The solution (8) of the GMTL method is correct only when the iterative calculations in the perturbation method are converged. The detailed discussions on the perturbation method and its convergence can be found in [8], and the key points are concluded here.

Assuming the original governing equation in matrix format is:

$$\left(\overline{\overline{A}} - \overline{\overline{\varepsilon}}\right) \cdot \overline{x} = \overline{b} \tag{9}$$

where matrix $\overline{\overline{\varepsilon}}$ is a small correction part of matrix $\overline{\overline{A}}$; $\overline{x}$ is the unknown vector to be solved; $\overline{b}$ is the known vector on the right-hand-side of the equation.

Then, the explicit solution of (9) can be written as:

$$\overline{x} = \left(\overline{\overline{A}} - \overline{\overline{\varepsilon}}\right)^{-1} \cdot \overline{b} \tag{10}$$

To solve (9) using the perturbation method:

For $n = 0$:

$$\overline{x}_{(0)} = \overline{\overline{A}}^{-1} \cdot \overline{b} \tag{11}$$

For $n \geqslant 1$:

$$\overline{x}_{(n)} = \overline{\overline{A}}^{-1} \overline{\overline{\varepsilon}} \cdot \overline{x}_{(n-1)} = \left(\overline{\overline{A}}^{-1} \overline{\overline{\varepsilon}}\right)^{n} \cdot \overline{\overline{A}}^{-1} \cdot \overline{b} \tag{12}$$

Thus, the solution of (9) from the perturbation method is:

$$\overline{x}_{p} = \sum_{n=0}^{\infty} \overline{x}_{(n)} = \left(\overline{\overline{I}} - \overline{\overline{A}}^{-1} \overline{\overline{\varepsilon}}\right)^{-1} \overline{\overline{A}}^{-1} \overline{b} \left[\overline{\overline{I}} - \left(\overline{\overline{A}}^{-1} \overline{\overline{\varepsilon}}\right)^{n+1}\right] \tag{13}$$

when $\left(\overline{\overline{I}} - \overline{\overline{A}}^{-1} \overline{\overline{\varepsilon}}\right)$ is not singular.

Comparing the explicit solution (10) and the solution from the perturbation method (13), it can be noticed that these two solutions will be the same after enough number of iterations in perturbation method if

$$\lim_{n\to\infty}\left(\overline{\overline{A}}^{-1}\overline{\overline{\varepsilon}}\right)^{n+1}=\overline{\overline{0}} \tag{14}$$

An $n\times n$ matrix $\overline{\overline{M}}$ has n eigenvalues λ_i (where $i = 1, 2, \dots, n$), and the spectral radius $\rho\left(\overline{\overline{M}}\right)$ of $\overline{\overline{M}}$ is defined as

$$\rho\left(\overline{\overline{M}}\right)=\max_{1\leqslant i\leqslant n}|\lambda_i| \tag{15}$$

Based on the theorem of convergence matrices, when the spectral radius $\rho\left(\overline{\overline{A}}^{-1}\overline{\overline{\varepsilon}}\right)<1$, (14) will be satisfied [9].

Therefore, it can be concluded that when the relation of matrices $\overline{\overline{A}}$ and $\overline{\overline{\varepsilon}}$ in the original equation (9) meets the condition that

$$\rho\left(\overline{\overline{A}}^{-1}\overline{\overline{\varepsilon}}\right)<1 \tag{16}$$

the perturbation method can be used to solve the original equation and the solution from the iterative calculation will converge to the explicit solution.

In the GMTL method, MNA (modified nodal analysis) method is implemented and the original equation (1) can be written in matrix format [5]:

$$\begin{bmatrix} j\omega\overline{\overline{C}} & \overline{\overline{\Lambda}}^{T} \\ -\overline{\overline{\Lambda}} & j\omega\overline{\overline{L}} \end{bmatrix}\cdot\begin{bmatrix}\overline{\phi} \\ \overline{i}\end{bmatrix}=\begin{bmatrix}\overline{E}^{inc} \\ \overline{0}\end{bmatrix}+\begin{bmatrix} j\omega\overline{\overline{D_C}} & \overline{\overline{0}} \\ \overline{\overline{0}} & j\omega\overline{\overline{D_L}} \end{bmatrix}\cdot\begin{bmatrix}\overline{\phi} \\ \overline{i}\end{bmatrix} \tag{17}$$

where $\overline{\overline{D_C}}$ and $\overline{\overline{D_L}}$ are the correction terms to compensate the differences between the classic MTL modeling and the full-wave mixed-potential integral equations.

In (17), let $\begin{bmatrix} j\omega\overline{\overline{C}} & \overline{\overline{\Lambda}}^{T} \\ -\overline{\overline{\Lambda}} & j\omega\overline{\overline{L}} \end{bmatrix}$ and $\begin{bmatrix} j\omega\overline{\overline{D_C}} & \overline{\overline{0}} \\ \overline{\overline{0}} & j\omega\overline{\overline{D_L}} \end{bmatrix}$ be $\overline{\overline{A}}$ and $\overline{\overline{\varepsilon}}$ in (9), respectively. Thus, it can be concluded that the iterative calculation in the GMTL method will converge if

$$\rho\left(\begin{bmatrix} j\omega\overline{\overline{C}} & \overline{\overline{\Lambda}}^{T} \\ -\overline{\overline{\Lambda}} & j\omega\overline{\overline{L}} \end{bmatrix}^{-1} \cdot \begin{bmatrix} j\omega\overline{\overline{D_C}} & \overline{\overline{0}} \\ \overline{\overline{0}} & j\omega\overline{\overline{D_L}} \end{bmatrix}\right) < 1 \tag{18}$$

The matrix $\begin{bmatrix} j\omega\overline{\overline{C}} & \overline{\overline{\Lambda}}^{T} \\ -\overline{\overline{\Lambda}} & j\omega\overline{\overline{L}} \end{bmatrix}$ is the original MNA matrix in the classic MTL method, and the matrix $\begin{bmatrix} j\omega\overline{\overline{D_C}} & \overline{\overline{0}} \\ \overline{\overline{0}} & j\omega\overline{\overline{D_L}} \end{bmatrix}$ is related to the differences between the MTL method and the MPIE method. Intuitively, the convergence requirement (18) is more likely to be satisfied when the differences are less significant compared to the original MTL modeling. In other words, if the differences to correct in the GMTL method are no longer a small portion compared to the classic MTL method, the convergence in the GMTL method will fail. This situation is more likely to happen near the resonant frequencies of the MTL system, because the radiation behavior is more dominant in the MTL system and the MTL model derived from the transmission-line theory is not able to take the radiation behavior into consideration. Therefore, the GMTL method has worse convergence characteristics when the solution frequency is closer to the MTL system resonant frequencies.

3. THE GMTL METHOD WITH RADIATION LOSS RESISTANCES

Based on the discussion in the previous section, a reasonable approach to improve the convergence characteristics of the GMTL method near the resonant frequencies of the

MTL system is to include the impacts of radiation in the MTL system in the MNA matrix representing the classic MTL method. By including the impacts of the radiation in the classic MTL matrix, the correction terms in the GMTL perturbation method will still be less dominant and the iterative calculation can have better convergence characteristics.

In [10] and [11], the equivalent resistances in the MTL system are introduced to quantify the radiation behavior, and the detailed derivations on the radiation loss resistances are presented in these references. As shown in Figure 1, the radiation loss resistances should be added as both the self-terms ($R_{rad,11}$ and $R_{rad,22}$) and the mutual terms ($R_{rad,m}$).

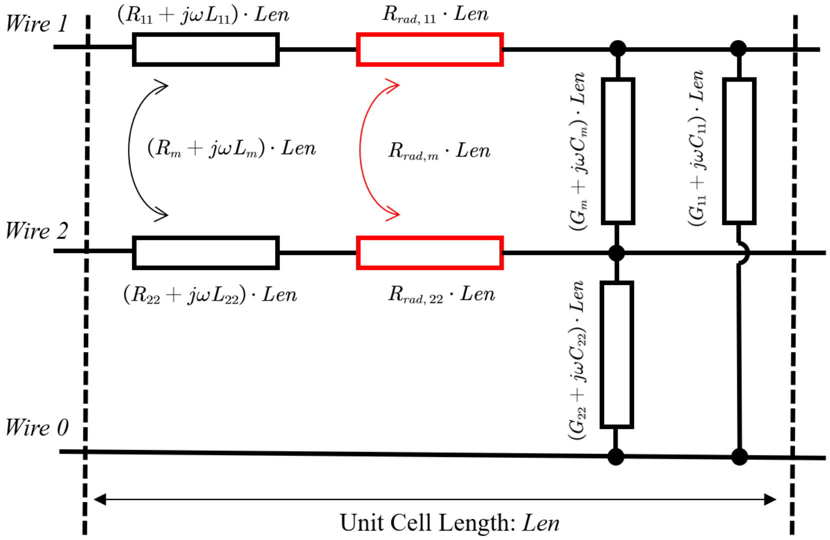

Figure 1. An example of adding radiation loss resistances in the original two-wire MTL unit cell.

The general formulation for the per-unit-length radiation loss resistances in matrix format is:

$$\left[\overline{\overline{R}}_{rad,pul}\right]=\left(\frac{1}{\omega^{2}}\left[\overline{\overline{S}}\right]\right)^{\frac{1}{2}}\left[\overline{\overline{C'}}\right]^{-1} \tag{19}$$

where

$$\begin{aligned}\left[\overline{\overline{S}}\right]=\omega^{2}\left[\overline{\overline{\alpha}}\right]\left[\overline{\overline{L'}}\right]\left[\overline{\overline{C'}}\right]\left[\overline{\overline{\alpha}}\right]+\left(\left[\overline{\overline{\alpha}}\right]\left[\overline{\overline{\beta}}\right]\right)^{2}+\left(\left[\overline{\overline{\beta}}\right]\left[\overline{\overline{\alpha}}\right]\right)^{2}\\+\left[\overline{\overline{\beta}}\right]\left[\overline{\overline{\alpha}}\right]^{2}\left[\overline{\overline{\beta}}\right]+\left[\overline{\overline{\alpha}}\right]^{4}-\left[\overline{\overline{\alpha}}\right]\left[\overline{\overline{R'}}\right]\left[\overline{\overline{G'}}\right]\left[\overline{\overline{\alpha}}\right]\end{aligned} \tag{20}$$

and $\left[\overline{\overline{\alpha}}\right]$ and $\left[\overline{\overline{\beta}}\right]$ are the real part and imaginary part of the matrix of propagation constant $\left[\overline{\overline{\gamma}}\right]$, respectively:

$$\left[\overline{\overline{\alpha}}\right]+j\left[\overline{\overline{\beta}}\right]=\left[\overline{\overline{\gamma}}\right]=\left\{\left(\left[\overline{\overline{R'}}\right]+j\omega\left[\overline{\overline{L'}}\right]\right)\left(\left[\overline{\overline{G'}}\right]+j\omega\left[\overline{\overline{C'}}\right]\right)\right\}^{\frac{1}{2}} \tag{21}$$

Also, the matrices $\left[\overline{\overline{R'}}\right]$, $\left[\overline{\overline{L'}}\right]$, $\left[\overline{\overline{G'}}\right]$ and $\left[\overline{\overline{C'}}\right]$ in (19) ~ (21) are the high-frequency transmission-line per-unit-length parameters introduced in [10] and [11].

After introducing the radiation loss resistances in the original MTL system, the equation in the GMTL method (17) will be updated as:

$$\begin{bmatrix} j\omega\overline{\overline{C}} & \overline{\overline{\Lambda}}^{T} \\ -\overline{\overline{\Lambda}} & j\omega\overline{\overline{L}}+\overline{\overline{R}}_{rad}\end{bmatrix}\cdot\begin{bmatrix}\bar{\phi}\\ \bar{i}\end{bmatrix}=\begin{bmatrix}\overline{E}^{inc}\\ \bar{0}\end{bmatrix}+\begin{bmatrix} j\omega\overline{\overline{D_{C}}} & \overline{\overline{0}} \\ \overline{\overline{0}} & j\omega\overline{\overline{D_{L}}}+\overline{\overline{R}}_{rad}\end{bmatrix}\cdot\begin{bmatrix}\bar{\phi}\\ \bar{i}\end{bmatrix} \tag{22}$$

4. NUMERICAL EXAMPLES

To validate the effectiveness of improving the convergence performance of the GMTL method by adding the additional radiation loss resistances, a four-wire MTL system with an ideal reference plane beneath the wires is introduced.

The cross-section of the MTL system is shown in Figure 2. There are two loops: the loop consisting with Wire 1 and Wire 2 is the aggressor loop with a voltage source excitation at one end of the loop; the loop consisting with Wire 3 and Wire 4 is the victim loop and is excited by the EM coupling with the aggressor loop. The length of each wire is 1.5 m, so the first resonant frequency of this MTL system is 100 MHz. Also, 0.1-Ohm resistive loads are added at all terminals of these 2 wire loops.

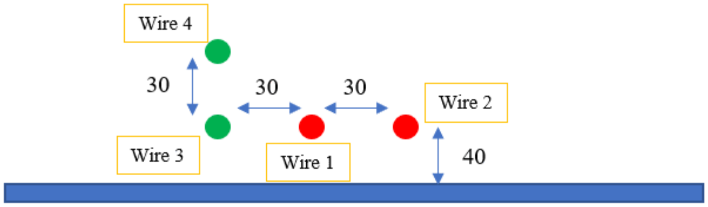

Figure 2. The geometry information of the cross-section of the four-wire system. (Unit: mm)

Using the example of the MTL system shown in Figure 2, the effectiveness of the proposed approach to improve the convergence characteristics of the GMTL method near the resonant frequencies can be validated. Since the first resonant frequencies of the MTL system is 100 MHz, so the current distributions on these wires are solved at 100 MHz and 200 MHz using (1) the classic MTL method, (2) the GMTL method, (3) the improved GMTL method with additional radiation loss resistors, and (4) the full-wave MPIE method, respectively. In addition, the wire current distributions are also calculated at another frequency, 135 MHz, which is far away from the resonant frequencies of the MTL system.

The comparisons on the wire current distributions at 100 MHz are shown in Figure 3, and the comparisons at 200 MHz are shown in Figure 4. In both Figure 3 and Figure 4, the upper two figures include the results from all four different calculation methods, where the results from the GMTL method (the purple dashed curves) have very large magnitudes. These large magnitudes on the calculated current distributions indicate that the iterative calculations in the GMTL method fail to converge at these resonant frequencies. The lower two figures in Figure 3 and Figure 4 are zoomed-in plots focused on the current distribution curves without the results from the GMTL method. At both resonant frequency points, certain discrepancies can be observed between the results from the classic MTL method and the full-wave MPIE results. However, the improved GMTL method with the additional radiation loss resistances gives well-matched results on the wire current distributions compared to the full-wave MPIE results.

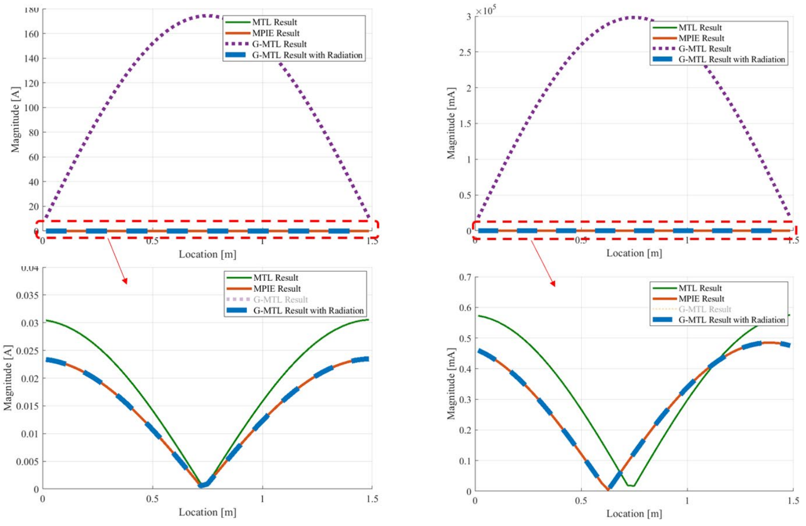

(a) (b)

Figure 3. The comparisons on the wire current distributions at 100 MHz: (a) the current distribution on Wire 1 in the aggressor loop; and (b) the current distribution on Wire 3 in the victim loop.

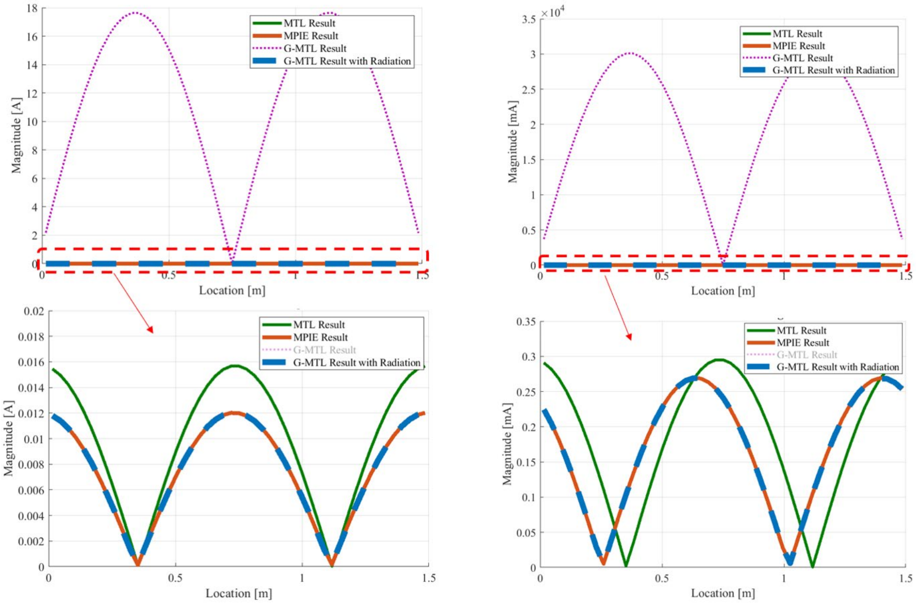

(a) (b)

Figure 4. The comparisons on the wire current distributions at 200 MHz: (a) the current distribution on Wire 1 in the aggressor loop; and (b) the current distribution on Wire 3 in the victim loop.

Also, the improvement on the convergence characteristics can be evaluated using (16). The values of the calculated spectral radius are summarized in Table 1. When solving the MTL system using the GMTL method, the values of the spectral radius are larger than 1, indicating that the iterative calculations are not converged. When solving the problem using the improved GMTL method, the spectral radius becomes less than 1 and the calculated results converge to the full-wave MPIE results. The results on the spectral radius are consistent with the observations on the convergence characteristics from Figure 3 and Figure 4.

In Figure 5, the current distributions are compared at 135 MHz, which is far away from the system resonant frequencies. Under this circumstance, the GMTL method do not have any convergence issues, and both the GMTL method and the improved GMTL method can correct the discrepancies between the results from the classic MTL method and the full-wave MPIE results.

Table 1. The Values of the Spectral Radius in the GMTL and the Improved GMTL Methods

Frequency [MHz]	100	200
Spectral Radius in the GMTL Method	27.60	17.51
Spectral Radius in the Improved GMTL Method	0.9983	0.9986

Therefore, it can be concluded that the convergence characteristics of the GMTL method near the resonant frequencies can be improved by adding the radiation loss resistances. Also, the solutions from the improved GMTL method have good correlations to the solutions from the full-wave MPIE method in the frequency bands both near and far away from the resonant frequencies of the MTL system.

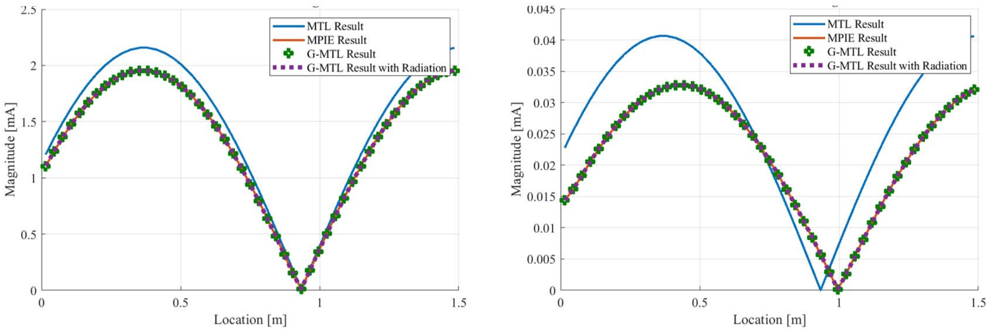

(a) (b)

Figure 5. The comparisons on the wire current distributions at 135 MHz: (a) the current distribution on Wire 1 in the aggressor loop; and (b) the current distribution on Wire 3 in the victim loop.

5. CONCLUSION

In this study, the convergence characteristics of the GMTL method near the resonant frequencies of the MTL system is improved by adding the radiation loss resistances in the MTL modeling. By calculating the spectral radius of the matrix in the GMTL governing equation, the convergence of the perturbation method can be determined before starting the GMTL iterative calculation. Then, the effectiveness of the improved GMTL method is validated through a numerical example. After adding the additional radiation loss resistances in the improved GMTL method, the discrepancies between the full-wave MPIE solution and the classic MTL solution can be corrected, and the convergence issue of the GMTL method no longer exists near the MTL system resonant frequencies.

REFERENCES

[1] H. Bagci, A. E. Yilmaz, J. -M. Jin and E. Michielssen, "Fast and Rigorous Analysis of EMC/EMI Phenomena on Electrically Large and Complex Cable-Loaded Structures," in IEEE Transactions on Electromagnetic Compatibility, vol. 49, no. 2, pp. 361-381, May 2007.

[2] M. Ouyang, X. Wang, N. Altunyurt, V. Sanphuang, N. Parsa and J. Fan, "Cable Harness Modeling Using MTL Parameters Derived from Integral Equations," *2020 IEEE International Conference on Computational Electromagnetics (ICCEM)*, Singapore, 2020, pp. 66-68.

[3] C. W. Ho, "Theory and Computer-aided Analysis of Lossless Transmission Lines," in *IBM Journal of Research and Development*, vol. 17, no. 3, pp. 249-255, May 1973.

[4] G. Muller, J. Wendei and K. Reiss, "Efficient analysis of coupled multiconductor transmission lines," *1999 International Symposium on Electromagnetic Compatibility (IEEE Cat. No.99EX147)*, 1999, pp. 646-649.

[5] Y. Wang, Y. S. Cao, D. Liu, R. W. Kautz, N. Altunyurt and J. Fan, "A Generalized Multiple-Scattering Method for Modeling a Cable Harness With Ground Connections to a Nearby Metal Surface," in *IEEE Transactions on Electromagnetic Compatibility*, vol. 61, no. 1, pp. 261-270, Feb. 2019.

[6] Y. Wang, Y. S. Cao, D. Liu, R. W. Kautz, N. Altunyurt and J. Fan, "Evaluating the Crosstalk Current and the Total Radiated Power of a Bent Cable Harness Using the Generalized MTL Method," in *IEEE Transactions on Electromagnetic Compatibility*, vol. 62, no. 4, pp. 1256-1265, Aug. 2020.

[7] S. Tkatchenko, F. Rachidi and M. Ianoz, "Electromagnetic field coupling to a line of finite length: theory and fast iterative solutions in frequency and time domains," in *IEEE Transactions on Electromagnetic Compatibility*, vol. 37, no. 4, pp. 509-518, Nov. 1995.

[8] Mark H Holmes, *Introduction to perturbation methods*, 2nd ed. New York, NY, USA: Springer, 2013.

[9] Burden, R.L. and Faires, J.D., *Numerical Analysis*. Boston, MA, USA: PWS, 1993, pp. 412.

[10] S. Chabane, P. Besnier and M. Klingler, "Enhanced transmission line theory: Frequency-dependent line parameters and their insertion in a classical transmission line equation solver," *2013 International Symposium on Electromagnetic Compatibility*, Brugge, Belgium, 2013, pp. 326-331.

[11] S. Chabane, P. Besnier and M. Klingler, "A Modified Enhanced Transmission Line Theory Applied to Multiconductor Transmission Lines," in *IEEE Transactions on Electromagnetic Compatibility*, vol. 59, no. 2, pp. 518-528, April 2017.

III. AN IMPROVEMENT ON THE MULTIPLE SCATTERING METHOD FOR EVALUATING CURRENT DISTRIBUTIONS ON CABLE HARNESS USING THE SUB-STRUCTURE ANALYSIS

ABSTRACT

In this paper, an approach to improve the Multiple Scattering method is proposed to simplify the process of evaluating the current distributions on cable harness with the presenting of nearby metal structures. In the Multiple Scattering method, the calculations are divided into two separate domains: the cable harness part and the nearby conductive surface structure part. The cable harness part is solved using the generalized multi-conductor transmission-line theory, and the nearby metal surface structures are solved using the full-wave MPIE method. The calculations in these two domains happen iteratively and alternately to correct the calculated current distributions step by step. By introducing the sub-structure analysis, the iterations between the cable harness part and the nearby surface part are no longer required, which simplifies the Multiple Scattering calculations. In addition, the calculation results and the convergence characteristics of the improved Multiple Scattering method are discussed based on several numerical examples. It has been discovered that if the Multiple Scattering method may have convergence issue under certain circumstances, and the criterion to determine if the calculations would converge is derived.

Keywords: Cable harness, Multiconductor transmission-line, Multiple scattering, Sub-structure analysis.

1. INTRODUCTION

Evaluating current distributions on cable harness accurately and efficiently in a complex system, like a vehicle or an airplane, is becoming more important nowadays, because more sensitive equipment are put together in a single system and are connected with cable harness [1, 2]. For example, an autonomous vehicle requires radars, cameras, or other sensing devices put at different locations of the vehicle to collect information and make correct decisions [3]. Most of the communications between these sensors and the data process unit are transmitted through the cable harness system. The cable harness system can have very complex geometry structures because a single wire bundle usually contains lots of wires; in addition, irregularly shaped metal structures with slots and bumps are common in a system and have their impacts on current distributions on nearby cable harness [4]. Therefore, complex meshing is required to solve a cable harness system using classic full-wave methods, like mixed-potential integral equations (MPIE), and the calculations will be very computational resource consuming [5].

To cut down the required computational resources for solving the current distributions in cable harness system considering the impacts from the nearby metal structures, the HybridMTL method was proposed [4, 6]. In the HybridMTL method, the cable harness system is segmented, and the equivalent RLGC circuit model for each individual segment is extracted based on the multiconductor transmission-line (MTL) theory, considering the cross-sectional geometries of both the cable harness and the nearby metal structures. Thus, an equivalent circuit model with lumped RLGC elements can be built and the cable harness current distributions can be obtained by solving the equivalent circuit model. The circuit solver is generally more efficient compared to full-wave methods. However, in the MTL theory, it is assumed that only the TEM mode exists in the system, which limits the accuracy of the analysis [7]. If the separations between wires or nearby metal structures in the cross section is electrically large, i.e., $\lambda/10$, neglecting the impacts from higher-order modes can introduce a significant amount of error [8, 9]. Also, near the resonant frequencies of the cable harness system, the level of radiation energy can be significantly higher, and the antenna-mode current becomes more dominant compared to the transmission-line-mode current. Using the circuit model derived from the MTL theory, only the transmission-line-mode current can be included and missing the antenna-mode current in the analysis results in larger discrepancies to the full-wave results [1, 10].

In [10], the Multiple Scattering method was proposed to solve the accuracy issue in the HybridMTL method. In the Multiple Scattering method, the whole system is divided into two separate parts: the cable harness and the nearby metal structures. When solving the cable harness part, the nearby metal structures are not considered in the calculation, and the generalized MTL method is implemented to solve the current distributions on the cable harness [6, 11]. Then, the scattered electromagnetic fields resulted from the cable harness currents are evaluated and serve as the incident fields when calculating the surface current distribution in the following step. The surface current distribution is solved using the MPIE method with the incident electromagnetic fields from the cable harness current. After getting the surface current distributions on nearby metal structures, the scattered electromagnetic fields from the nearby surface currents can also be calculated. Then, the calculation goes to the cable harness part again and the generalized MTL method will use the scattered fields from the surface currents as the incident excitations. The calculations for the cable harness part using the generalized MTL method and the calculations for the nearby metal surface part using the MPIE method happen iteratively and alternately to correct the cable harness current step by step. The advantage of the Multiple Scattering method is that less computational resources are required compared to using full-wave methods to solve the whole model including cable harness and nearby metal surfaces together.

The idea of sub-structure analysis method was first proposed in [12], and it was developed to simplify the analysis on the characteristic mode, making the investigations on the radiation characteristics of a structure more efficient. Despite of the fact that the sub-structure method was developed for studying the radiation behavior, the same mathematics can be implemented to other problems related to matrix calculations. An example of using sub-structure analysis in MTL investigation has been demonstrated in [4].

In this study, evaluating the current distributions on cable harness using the Multiple Scattering method is improved with the sub-structure analysis, and the perturbation method is used to solve the cable harness problem iteratively. The advantage of this perturbation method is that the matrix equation to solve has the same format as an ordinary MTL problem, where the inverse matrix calculation is on a sparse matrix and less calculation resources are required compared to inversing a dense matrix when solving a general MPIE problem. In addition, the requirement for the convergence of the perturbation calculations is discussed.

The organization of this paper is briefly summarized here. In Section II, the generalized MTL method and the Multiple Scattering method are briefly reviewed. In Section III, the sub-structure analysis method for a cable harness system with nearby metal structures are discussed. In Section IV, the improved Multiple Scattering with the sub-structure analysis using the perturbation method is proposed. In Section V, the proposed Multiple Scattering method is demonstrated using a numerical example. In Section VI, the convergence characteristics of the proposed improved Multiple Scattering method and the criterion to determine the convergence are discussed. In Section VII, discussions and conclusions of this paper are given.

2. REVIEW ON THE GENERALIZED MTL METHOD AND MULTIPLE SCATTERING METHOD

The generalized MTL method is proposed in [6] and the Multiple Scattering method is introduced in [1, 10]. The detailed information can be found in those reference papers, and these two methods are briefly introduced in this section.

2.1. REVIEW ON THE GENERALIZED MTL METHOD

The governing equations of the generalized MTL method are

$$\begin{cases} \frac{d}{dl}\bar{\phi} + j\omega\bar{\bar{L}}\bar{i} = \bar{E}^{inc} + j\omega\bar{D}_1\left\{\bar{i}\right\} \\ \frac{d}{dl}\bar{i} + j\omega\bar{\bar{C}}\bar{\phi} = \bar{D}_2\left\{\bar{i}\right\} \end{cases} \tag{1}$$

where $\bar{\phi}$, $\bar{i}$ and $\bar{E}^{inc}$ are the vectors of the electrical potential, the current and the incident electrical field on the wires in the MTL system, respectively.

There are two correction terms, $\bar{D}_1\left\{\bar{i}\right\}$ and $\bar{D}_2\left\{\bar{i}\right\}$, in (1) compared to the equations when solving an original MTL system. After adding these two correction terms, the discrepancies between the classic transmission-line modeling and the full-wave MPIE methods. Therefore, the expressions for these correction terms are:

$$\bar{D}_1\left\{\bar{i}\right\} = \bar{\bar{L}}\,\bar{i} - \bar{A} \tag{2}$$

$$\bar{D}_2\left\{\bar{i}\right\} = \frac{d}{dl}\bar{i} - \bar{\bar{C}}\,\bar{P} \tag{3}$$

At the observation location $\vec{r}$, $\bar{A}(\vec{r})$ and $\bar{P}(\vec{r})$ in (2) and (3) can be calculated by

$$A\left(\vec{r}\right) = \mu\int_{l} i(\vec{r}\,')\,g(\vec{r},\vec{r}\,')\,d\vec{r}\,' \tag{4}$$

$$\bar{P}(\vec{r}) = \frac{1}{\varepsilon}\int_{l} \frac{d}{dl'}\, i(\vec{r}\,')\,g(\vec{r},\vec{r}\,')\,d\vec{r}\,' \tag{5}$$

Also, these two correction terms have unknown parameters $\bar{i}$ and are added on the right-hand side of the equations. Thus, the left-hand side of (1) keeps the same format compared to the original MTL equations.

Then, the current and potential distributions on the wires can be calculated iteratively using the perturbation method. At the initial step of calculation, $n = 0$, the correction terms are not considered in the calculation, and the equations to solve are:

$$\begin{cases} \dfrac{d}{dl}\bar{\phi}_{(n)} + j\omega\bar{\bar{L}}\,\bar{i}_{(n)} = \bar{E}^{inc} \\ \dfrac{d}{dl}\bar{i}_{(n)} + j\omega\bar{\bar{C}}\,\bar{\phi}_{(n)} = \bar{0} \end{cases} \tag{6}$$

In the following steps of iterations ($n \geqslant 1$), only the correction terms are included on the right-hand side of the equations, and the equations to solve are:

$$\begin{cases} \frac{d}{dl}\bar{\phi}_{(n)} + j\omega \bar{\bar{L}}\,\bar{i}_{(n)} = j\omega \bar{D}_1\left\{\bar{i}_{(n-1)}\right\} \\ \frac{d}{dl}\bar{i}_{(n)} + j\omega \bar{\bar{C}}\,\bar{\phi}_{(n)} = \bar{D}_2\left\{\bar{i}_{(n-1)}\right\} \end{cases} \tag{7}$$

And the final solution of (1) from the perturbation method can be calculated by the summation of the solutions from each iteration steps:

$$\begin{cases} \bar{\phi} = \sum_{n=0}^{\infty} \bar{\phi}_{(n)} \\ \bar{i} = \sum_{n=0}^{\infty} \bar{i}_{(n)} \end{cases} \tag{8}$$

If the perturbation calculation is converged, the solution from (8) will be the same compared to the original MPIE method.

2.2. REVIEW ON THE MULTIPLE SCATTERING METHOD

When solving the current distributions on cable harness using the Multiple Scattering method, the steps of calculations can be found in the diagram shown in Figure 1, and these steps are explained in detail here.

Step 1: Excite the cable harness system with the lumped sources on wire and calculate the cable harness current distribution $i_{wire}^{(0)}$ using the generalized MTL method. As introduced in the previous section, the cable harness current distribution $i_{wire}^{(0)}$ is calculated iteratively using the perturbation method using (1) ~ (8).

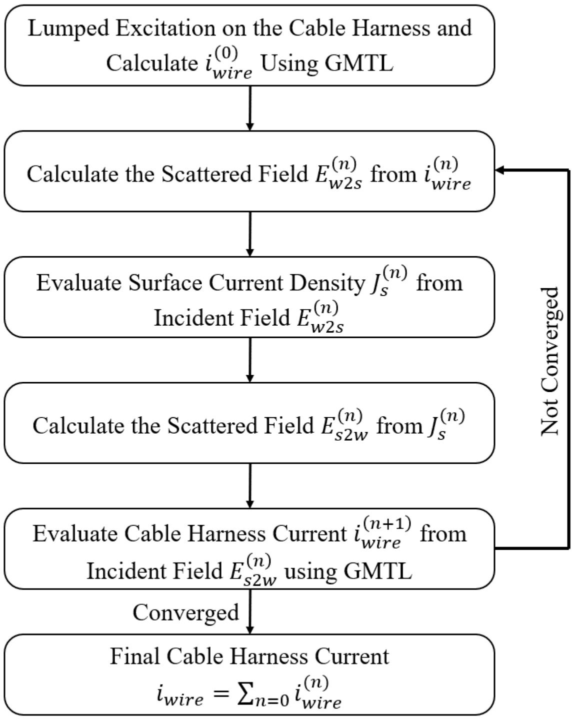

Figure 1. The diagram for the calculation steps of the Multiple Scattering method.

Step 2: Calculate the field $E_{w2s}^{(n)}$ resulting from the cable harness currents $i_{wire}^{(n)}$. The field $E_{w2s}^{(n)}$ scatters from the cable harness to the nearby metal surface and becomes the incident field when calculating the surface currents in the next step.

Step 3: Evaluate the surface current density distribution $J_s^{(n)}$ on the nearby metal surface generated by the incident field $E_{w2s}^{(n)}$ calculated in the previous step.

Step 4: Calculate the scattered field $E_{s2w}^{(n)}$ resulting from the surface current density on the nearby metal surface $J_s^{(n)}$. The scattered field $E_{s2w}^{(n)}$ is the incident field excitation for the cable harness current evaluation in the next iteration step $i_{wire}^{(n+1)}$.

Step 5: Calculate the cable harness current distribution in the next step of iteration $i_{wire}^{(n+1)}$. In this calculation, the lumped excitation on cable harness in the initial cable current calculation $i_{wire}^{(0)}$ is no longer included, and the excitation is the field scattered back from the induced surface currents.

Step 6: Update the cable harness current distribution results based on the perturbation method, and check if the calculated results have converged or not. The current distribution can be calculated by the summation of all the previously calculated cable harness currents:

$$i_{wire} = \sum_{n=0} i_{wire}^{(n)} \tag{9}$$

Step 7: if the calculated current distribution meets the pre-set convergence requirements, the final solution for the cable harness current distributions can be determined; if the convergence requirements are not satisfied, one more time of iteration calculation ($n = n + 1$) will be taken from Step 2 to Step 6.

As discussed in the previous section, to calculate the cable harness current distributions from the perturbation method iteratively, the currents calculated in each individual iteration step are summed up to get the final results. Therefore, in the Multiple Scattering method, the amount of modifications on the calculation results in the new iteration step is $i_{wire}^{(n+1)}$:

$$i_{wire,new} = \sum_{n=0} i_{wire}^{(n)} = i_{wire,old} + i_{wire}^{(n+1)} \tag{10}$$

If the maximum value of the wire current elements in $i_{wire}^{(n+1)}$ is smaller than a pre-determined threshold value, it can be concluded that the iterative calculations are converged at this stage.

In this section, the generalized MTL method and the Multiple Scattering method have been reviewed briefly, and more details can be found in the listed reference paper. Based on these understandings, it can be noticed that the Multiple Scattering method corrects the cable harness current distributions using the iterative perturbation calculations, and in each perturbation step of the Multiple Scattering calculation, the cable harness current distributions are calculated using the generalized MTL method, which is also an iterative process. Thus, there are two kinds of iterative calculation steps in the Multiple Scattering method, and the algorithm can be simplified and the required time can be reduced if these iterative calculation processes can be properly optimized.

3. SUB-STRUCTURE ANALYSIS METHOD

The sub-structure analysis method was first developed to simplify the analysis on the characteristic modes of a complex structure which can be divided into different parts, and to study the radiation characteristics of the structure.

In a cable harness system with nearby metal structure, the whole system is also possible to be divided into two different parts: the cable harness part and the nearby metal surface part. Therefore, there are possibilities to simplify the analysis on the cable harness system using the similar mathematical process as the sub-structure analysis.

An example of a cable harness system with nearby metal surface is shown in Figure 2. Let the cable harness part be the "*H*" part and the nearby metal surface part be the "*P*" part. As introduced in [10], the original matrix format equation to solve the MPIEs with modified modal analysis (MNA) method is

$$\begin{bmatrix} j\omega\overline{\overline{C}} & \overline{\overline{\Lambda}}^{T} \\ -\overline{\overline{\Lambda}} & j\omega\overline{\overline{L}} \end{bmatrix} \cdot \begin{bmatrix} \overline{\phi} \\ \overline{i} \end{bmatrix} = \begin{bmatrix} -\overline{I}^{e} \\ \overline{v}^{e} \end{bmatrix} \tag{11}$$

where $\overline{\overline{C}}$ and $\overline{\overline{L}}$ are the matrices of partial capacitances and partial inductances calculated by the integral equations, respectively [1]; $\overline{\overline{\Lambda}}$ is the connectivity matrix and it defines the relationship of connections between the partial capacitances and partial inductances; $\overline{I}^{e}$ and $\overline{v}^{e}$ are the vectors of the external current and voltage excitation sources; $\overline{\phi}$ and $\overline{i}$ are the unknown vectors of the potential and currents to be solved, respectively.

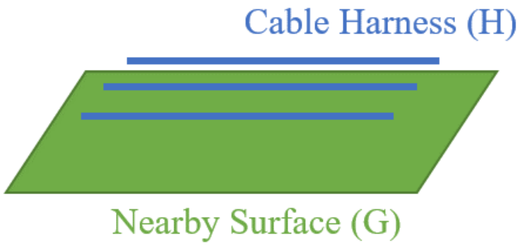

Figure 2. An example of a cable harness system with nearby metal surface.

Then, the matrices in (11) can be separated based on the cable harness part and the nearby metal surface part:

$$\overline{\overline{C}} = \begin{bmatrix} \overline{\overline{C}}_{GG} & \overline{\overline{C}}_{GH} \\ \overline{\overline{C}}_{HG} & \overline{\overline{C}}_{HH} \end{bmatrix} \tag{12}$$

$$\overline{\overline{L}} = \begin{bmatrix} \overline{\overline{L}}_{GG} & \overline{\overline{L}}_{GH} \\ \overline{\overline{L}}_{HG} & \overline{\overline{L}}_{HH} \end{bmatrix} \tag{13}$$

$$\overline{\overline{\Lambda}} = \begin{bmatrix} \overline{\overline{\Lambda}}_{GG} & \overline{\overline{\Lambda}}_{GH} \\ \overline{\overline{\Lambda}}_{HG} & \overline{\overline{\Lambda}}_{HH} \end{bmatrix} \tag{14}$$

$$\overline{\phi}=\left[\overline{\phi}_G^T\ \ \overline{\phi}_H^T\right]^T \tag{15}$$

$$\bar{i}=\left[\bar{i}_G^T\ \ \bar{i}_H^T\right]^T \tag{16}$$

$$\overline{I}^e=\left[\overline{I}_G^{e\,T}\ \ \overline{I}_H^{e\,T}\right] \tag{17}$$

$$\overline{v}^e=\left[\overline{v}_G^{e\,T}\ \ \overline{v}_H^{e\,T}\right]^T \tag{18}$$

and (11) can be written as:

$$j\omega\cdot\begin{bmatrix}\overline{\overline{C}}_{GG} & \overline{\overline{C}}_{GH}\\ \overline{\overline{C}}_{HG} & \overline{\overline{C}}_{HH}\end{bmatrix}\cdot\begin{bmatrix}\overline{\phi}_G\\ \overline{\phi}_H\end{bmatrix}+\begin{bmatrix}\overline{\overline{\Lambda}}_{GG}^T & \overline{\overline{\Lambda}}_{HG}^T\\ \overline{\overline{\Lambda}}_{GH}^T & \overline{\overline{\Lambda}}_{HH}^T\end{bmatrix}\cdot\begin{bmatrix}\bar{i}_G\\ \bar{i}_H\end{bmatrix}=\begin{bmatrix}-\overline{I}_G^e\\ -\overline{I}_H^e\end{bmatrix} \tag{19}$$

and

$$-\begin{bmatrix}\overline{\overline{\Lambda}}_{GG} & \overline{\overline{\Lambda}}_{GH}\\ \overline{\overline{\Lambda}}_{HG} & \overline{\overline{\Lambda}}_{HH}\end{bmatrix}\cdot\begin{bmatrix}\overline{\phi}_G\\ \overline{\phi}_H\end{bmatrix}+j\omega\cdot\begin{bmatrix}\overline{\overline{L}}_{GG} & \overline{\overline{L}}_{GH}\\ \overline{\overline{L}}_{HG} & \overline{\overline{L}}_{HH}\end{bmatrix}\cdot\begin{bmatrix}\bar{i}_G\\ \bar{i}_H\end{bmatrix}=\begin{bmatrix}\overline{v}_G^e\\ \overline{v}_H^e\end{bmatrix} \tag{20}$$

where the subscriptions with the same letters, i.e., "*GG*" and "*HH*", indicate that the matrices are associated with elements within the same part of the divided model; and the subscriptions with different letters, i.e., "*GH*" and "*HG*", indicate that the matrices are associated with elements between different the cable harness part and the nearby metal surface part.

Another thing to note is that, from the integral equations, the partial inductance matrix and the partial potential coefficient matrix can be calculated, and the partial capacitance matrix is calculated by the inverse of the partial potential coefficient matrix:

$$\begin{aligned}\begin{bmatrix}\overline{\overline{C}}_{GG} & \overline{\overline{C}}_{GH}\\ \overline{\overline{C}}_{HG} & \overline{\overline{C}}_{HH}\end{bmatrix}&=\begin{bmatrix}\overline{\overline{K}}_{GG} & \overline{\overline{K}}_{GH}\\ \overline{\overline{K}}_{HG} & \overline{\overline{K}}_{HH}\end{bmatrix}^{-1}\\ &=\begin{bmatrix}\left(\overline{\overline{K}}_{GG}-\overline{\overline{K}}_{GH}\overline{\overline{K}}_{HH}^{-1}\overline{\overline{K}}_{HG}\right)^{-1} & -\left(\overline{\overline{K}}_{GG}-\overline{\overline{K}}_{GH}\overline{\overline{K}}_{HH}^{-1}\overline{\overline{K}}_{HG}\right)^{-1}\overline{\overline{K}}_{GH}\overline{\overline{K}}_{HH}^{-1}\\ -\left(\overline{\overline{K}}_{HH}-\overline{\overline{K}}_{HG}\overline{\overline{K}}_{GG}^{-1}\overline{\overline{K}}_{GH}\right)^{-1}\overline{\overline{K}}_{HG}\overline{\overline{K}}_{GG}^{-1} & \left(\overline{\overline{K}}_{HH}-\overline{\overline{K}}_{HG}\overline{\overline{K}}_{GG}^{-1}\overline{\overline{K}}_{GH}\right)^{-1}\end{bmatrix}\end{aligned} \tag{21}$$

Assume that there is no external excitation on the nearby surface part:

$$\begin{cases} \overline{I}^{e}_{G} = \overline{0} \\ \overline{v}^{e}_{G} = \overline{0} \end{cases} \tag{22}$$

Then, the equation to calculate the unknown parameters related with the cable harness part can be derived from (19) to (22):

$$\begin{cases} \overline{i}_{G} = \overline{\overline{M}}_{1} \cdot \overline{\phi}_{H} + \overline{\overline{M}}_{2} \cdot \overline{i}_{H} \\ \overline{\phi}_{G} = \overline{\overline{M}}_{3} \cdot \overline{\phi}_{H} + \overline{\overline{M}}_{4} \cdot \overline{i}_{H} \end{cases} \tag{23}$$

where

$$\begin{cases} \overline{\overline{M}}_{1} = \left(\frac{1}{j\omega}\overline{\overline{\Lambda}}_{GG}\overline{\overline{C}}^{-1}_{GG}\overline{\overline{\Lambda}}^{T}_{GG} + j\omega\overline{\overline{L}}_{GG}\right)^{-1}\left(\overline{\overline{\Lambda}}_{GH} - \overline{\overline{\Lambda}}_{GG}\overline{\overline{C}}^{-1}_{GG}\overline{\overline{C}}_{GH}\right) \\ \overline{\overline{M}}_{2} = -\left(\frac{1}{j\omega}\overline{\overline{\Lambda}}_{GG}\overline{\overline{C}}^{-1}_{GG}\overline{\overline{\Lambda}}^{T}_{GG} + j\omega\overline{\overline{L}}_{GG}\right)^{-1}\left(\frac{1}{j\omega}\overline{\overline{\Lambda}}_{GG}\overline{\overline{C}}^{-1}_{GG}\overline{\overline{\Lambda}}^{T}_{HG} + j\omega\overline{\overline{L}}_{GH}\right) \\ \overline{\overline{M}}_{3} = -\overline{\overline{C}}^{-1}_{GG}\overline{\overline{C}}_{GH} - \frac{1}{j\omega}\overline{\overline{C}}^{-1}_{GG}\overline{\overline{\Lambda}}^{T}_{GG}\overline{\overline{M}}_{1} \\ \overline{\overline{M}}_{4} = -\frac{1}{j\omega}\overline{\overline{C}}^{-1}_{GG}\overline{\overline{\Lambda}}^{T}_{GG}\overline{\overline{M}}_{2} - \frac{1}{j\omega}\overline{\overline{C}}^{-1}_{GG}\overline{\overline{\Lambda}}^{T}_{HG} \end{cases} \tag{24}$$

and

$$\begin{bmatrix} \overline{\overline{N}}_{1} & \overline{\overline{N}}_{2} \\ \overline{\overline{N}}_{3} & \overline{\overline{N}}_{4} \end{bmatrix} \cdot \begin{bmatrix} \overline{\phi}_{H} \\ \overline{i}_{H} \end{bmatrix} = \begin{bmatrix} -\overline{I}^{e}_{H} \\ \overline{v}^{e}_{H} \end{bmatrix} \tag{25}$$

where

$$\begin{cases} \overline{\overline{N}}_{1} = j\omega\overline{\overline{C}}_{HG}\overline{\overline{M}}_{3} + j\omega\overline{\overline{C}}_{HH} + \overline{\overline{\Lambda}}^{T}_{GH}\overline{\overline{M}}_{1} \\ \overline{\overline{N}}_{2} = j\omega\overline{\overline{C}}_{HG}\overline{\overline{M}}_{4} + \overline{\overline{\Lambda}}^{T}_{GH}\overline{\overline{M}}_{2} + \overline{\overline{\Lambda}}^{T}_{HH} \\ \overline{\overline{N}}_{3} = -\overline{\overline{\Lambda}}_{HG}\overline{\overline{M}}_{3} - \overline{\overline{\Lambda}}_{HH} + j\omega\overline{\overline{L}}_{HG}\overline{\overline{M}}_{1} \\ \overline{\overline{N}}_{4} = -\overline{\overline{\Lambda}}_{HG}\overline{\overline{M}}_{4} + j\omega\overline{\overline{L}}_{HG}\overline{\overline{M}}_{2} + j\omega\overline{\overline{L}}_{HH} \end{cases} \tag{26}$$

The sub-structure analysis method is based on the assumption (22) that there is no excitation on one part of the model (nearby surface part in Figure 2). Generally, this assumption is true for most of the cable harness problems because the sources and loads are usually on the terminals of the cable harness.

After the mathematical conversion using the sub-structure analysis method, the dimensions of (25) reduce a lot compared to the original equation (11) because the unknown parameters in the updated equation are only related with the cable harness elements, and normally there are a large number of mesh elements on the nearby surface structures when solving using full-wave methods. The complexity of the matrix equation to solve a cable harness system with nearby metal surface is possible to be reduced with the help of sub-structure analysis.

4. THE IMPROVEMENT ON THE MULTIPLE SCATTERED METHOD

The fundamental formulations for the sub-structure analysis method have been introduced in the previous section. Using the sub-structure analysis method can reduce the complexity of the equation to solve a cable harness problem with nearby metal surface structures. Although the dimension of (25) is much less compared to the original matrix equation (11), but matrix calculations are still required to get the parameters $\overline{\overline{N}}_1$, $\overline{\overline{N}}_2$, $\overline{\overline{N}}_3$ and $\overline{\overline{N}}_4$ in the sub-structure equation (25). Also, in a typical MTL MNA matrix

$$\begin{bmatrix} j\omega\overline{\overline{C}}_{MTL} & \overline{\overline{\Lambda}}^T \\ -\overline{\overline{\Lambda}} & j\omega\overline{\overline{L}}_{MTL} \end{bmatrix} \cdot \begin{bmatrix} \overline{\phi} \\ \overline{i} \end{bmatrix} = \begin{bmatrix} -\overline{I}^e \\ \overline{v}^e \end{bmatrix} \tag{27}$$

the capacitance matrix $\overline{\overline{C}}_{MTL}$ and the inductance matrix $\overline{\overline{L}}_{MTL}$ are sparse matrices because only the self-terms and the mutual coupling terms between wire elements at the same cross section location. The coupling between wire elements at different locations are neglected in the MTL analysis. If the matrix $\begin{bmatrix}\overline{\overline{N}}_1 & \overline{\overline{N}}_2 \\ \overline{\overline{N}}_3 & \overline{\overline{N}}_4\end{bmatrix}$ in (25) can also be converted to a sparse matrix similar to the MTL MNA matrix, the solution for the sub-structure equation can be less computational resource intensive.

To make (25) from the sub-structure analysis have similar style compared to the MTL MNA equation, correction terms have to be added on the right-hand side of (25) to compensate the modifications made on the left-hand side of the equation.

Based on this idea, the sub-structure analysis can be introduced into the previous Multiple Scattering method to solve the current distributions on cable harness. The improved Multiple Scattering method is also based on the perturbation method and solve the cable harness current distribution iteratively. The equation to solve the system using the improved Multiple Scattering method is:

$$\begin{bmatrix} j\omega\cdot\overline{\overline{K}}^{-1}_{HH} & \overline{\overline{\Lambda}}^{T}_{HH} \\ -\overline{\overline{\Lambda}}_{HH} & j\omega\cdot\overline{\overline{L}}_{HH}\end{bmatrix}\cdot\begin{bmatrix}\overline{\phi}_H \\ \bar{i}_H\end{bmatrix} = \begin{bmatrix} -\overline{I}^{e}_H \\ \overline{v}^{e}_H\end{bmatrix} + \begin{bmatrix} j\omega\cdot\overline{D}_1\left\{\overline{\phi}_H\right\}+\overline{D}_2\left\{\bar{i}_H\right\}+\overline{D}_5\left\{\bar{i}_H\right\} \\ \overline{D}_3\left\{\overline{\phi}_H\right\}+j\omega\cdot\overline{D}_4\left\{\bar{i}_H\right\}+j\omega\cdot\overline{D}_6\left\{\bar{i}_H\right\}\end{bmatrix} \tag{28}$$

where $\overline{\overline{K}}_{HH}$ is the partial potential coefficient matrix, which is the inverse of the partial capacitance matrix $\overline{\overline{C}}_{HH}$; $\overline{D}_1\left\{\overline{\phi}_H\right\}$, $\overline{D}_2\left\{\bar{i}_H\right\}$, $\overline{D}_3\left\{\overline{\phi}_H\right\}$ and $\overline{D}_4\left\{\bar{i}_H\right\}$ are the correction terms to compensate the differences between the MTL-style matrix on the left-hand side of (28) and the left-hand side matrix from the sub-structure analysis method in (25); $\overline{D}_5\left\{\bar{i}_H\right\}$ and $\overline{D}_6\left\{\bar{i}_H\right\}$ are the correction terms in the generalized MTL method [11]. Therefore, in (28), the left-hand side matrix $\begin{bmatrix} j\omega\cdot\overline{\overline{K}}^{-1}_{HH} & \overline{\overline{\Lambda}}^{T}_{HH} \\ -\overline{\overline{\Lambda}}_{HH} & j\omega\cdot\overline{\overline{L}}_{HH}\end{bmatrix}$ is a sparse matrix and the elements are the same compared to the matrix when solving a general MTL problem using the MNA method in (27).

Then, the steps of the improved Multiple Scattering method are summarized below:

Step 1: calculate the MTL parameters and build the sparse matrix on the left-hand side of (28). The detailed derivations on these formulations can be found in [14]. The MTL capacitance and inductance can be calculated using the two-dimensional static analytical method based on the cross-sectional geometry.

The per-unit-length potential coefficient can be calculated by:

$$K_{ij} = -\frac{1}{4\pi\varepsilon}\ln\left(\rho_{ij}^2\right) \tag{29}$$

and the per-unit-length capacitance matrix can be calculated by

$$\overline{\overline{C}} = \overline{\overline{K}}^{-1} \tag{30}$$

The per-unit-length inductance can be calculated by:

$$L_{ij} = -\frac{\mu}{4\pi}\ln\left(\rho_{ij}^2\right) \tag{31}$$

The thin-wire assumption has been applied to derive the formulation (29) ~ (31). Also, i and j in (29) ~ (31) represent the numbers of wires in the MTL system. When $i = j$, K_{ij} and L_{ij} are the partial self-potential coefficient and partial self-inductance, respectively; when $i \neq j$, K_{ij} and L_{ij} are the partial mutual potential coefficient and partial mutual inductance, respectively.

Also,

$$\rho_{ij} = \begin{cases} a_i, & i = j \\ d_{ij}, & i \neq j \end{cases} \tag{32}$$

where a_i is the radius of wire i and d_{ij} is the center-to-center separation between wire i and wire j, as shown in Figure 3. In the thin-wire assumption, $a_i \ll d_{ij}$.

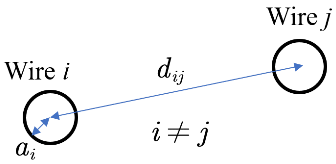

Figure 3. The cross-section geometry of wire i and wire j.

As introduced in [11], additional resistances can be added into the MTL model to include the radiation loss in the MTL system and the convergence characteristics of the perturbation method near the resonant frequencies of a cable harness system can be improved. The detailed discussions on the convergence characteristics and the calculation of the radiation loss resistances can be found in [11], [14] and [15], and the formulations to calculate the per-unit-length radiation loss resistances are summarized below in matrix format:

$$\left[\overline{\overline{R}}_{rad,pul}\right] = \left(\frac{1}{\omega^2}\left[\overline{\overline{S}}\right]\right)^{\frac{1}{2}}\left[\overline{\overline{C'}}\right]^{-1} \tag{33}$$

where

$$\begin{aligned}\left[\overline{\overline{S}}\right] = {} & \omega^2\left[\overline{\overline{\alpha}}\right]\left[\overline{\overline{L'}}\right]\left[\overline{\overline{C'}}\right]\left[\overline{\overline{\alpha}}\right] + \left(\left[\overline{\overline{\alpha}}\right]\left[\overline{\overline{\beta}}\right]\right)^2 + \left(\left[\overline{\overline{\beta}}\right]\left[\overline{\overline{\alpha}}\right]\right)^2 \\ & + \left[\overline{\overline{\beta}}\right]\left[\overline{\overline{\alpha}}\right]^2\left[\overline{\overline{\beta}}\right] + \left[\overline{\overline{\alpha}}\right]^4 - \left[\overline{\overline{\alpha}}\right]\left[\overline{\overline{R'}}\right]\left[\overline{\overline{G'}}\right]\left[\overline{\overline{\alpha}}\right]\end{aligned} \tag{34}$$

and $\left[\overline{\overline{\alpha}}\right]$ and $\left[\overline{\overline{\beta}}\right]$ are the real part and imaginary part of the matrix of propagation constant $\left[\overline{\overline{\gamma}}\right]$, respectively:

$$\left[\overline{\overline{\alpha}}\right]+j\left[\overline{\overline{\beta}}\right]=\left[\overline{\overline{\gamma}}\right]=\left\{\left(\left[\overline{\overline{R'}}\right]+j\omega\left[\overline{\overline{L'}}\right]\right)\left(\left[\overline{\overline{G'}}\right]+j\omega\left[\overline{\overline{C'}}\right]\right)\right\}^{\frac{1}{2}} \tag{35}$$

Also, the matrices $\left[\overline{\overline{R'}}\right]$, $\left[\overline{\overline{L'}}\right]$, $\left[\overline{\overline{G'}}\right]$ and $\left[\overline{\overline{C'}}\right]$ in (33) ~ (35) are the high-frequency transmission-line per-unit-length parameters introduced in [14] and [15].

Step 2: calculate the correction terms in (28). There are six correction terms in (28), and the two terms related with the generalized MTL method can be calculated using the same formulations from (1) to (7).

For the other four correction terms $\overline{D}_1\left\{\overline{\phi}_H\right\}$, $\overline{D}_2\left\{\overline{i}_H\right\}$, $\overline{D}_3\left\{\overline{\phi}_H\right\}$ and $\overline{D}_4\left\{\overline{i}_H\right\}$ generated from the sub-structure analysis, they can be calculated by

$$\overline{D}_1\left\{\overline{\phi}_H\right\}=\left\{\begin{array}{c} \overline{\overline{K}}_{HH}^{-1}+\overline{\overline{Mat}}_{HH}^{-1}\overline{\overline{K}}_{HG}\overline{\overline{K}}_{GG}^{-1}\overline{\overline{K}}_{GH}\overline{\overline{K}}_{HH}^{-1} \\ -\overline{\overline{Mat}}_{HH}^{-1}-\left[\overline{\overline{\Lambda}}_{GH}^{T}+\overline{\overline{Mat}}_{HH}^{-1}\overline{\overline{K}}_{HG}\overline{\overline{K}}_{GG}^{-1}\overline{\overline{Mat}}_{GG}^{-1}\overline{\overline{\Lambda}}_{GG}^{T}\right] \\ \cdot\left[-\omega^2\overline{\overline{L}}_{GG}+\overline{\overline{\Lambda}}_{GG}\overline{\overline{Mat}}_{GG}\overline{\overline{\Lambda}}_{GG}^{T}\right]^{-1} \\ \cdot\left(\overline{\overline{\Lambda}}_{GH}+\overline{\overline{\Lambda}}_{GG}\overline{\overline{K}}_{GH}\overline{\overline{K}}_{HH}^{-1}\right) \end{array}\right\}\cdot\overline{\phi}_H \tag{36}$$

$$\overline{D}_2\left\{\overline{i}_H\right\}=\left\{\begin{array}{c} \left[\overline{\overline{Mat}}_{HH}^{-1}\overline{\overline{K}}_{HG}\overline{\overline{K}}_{GG}^{-1}\overline{\overline{Mat}}_{GG}\overline{\overline{\Lambda}}_{GG}^{T}+\overline{\overline{\Lambda}}_{GH}^{T}\right] \\ \cdot\left[j\omega\overline{\overline{L}}_{GG}+\dfrac{1}{j\omega}\overline{\overline{\Lambda}}_{GG}\overline{\overline{Mat}}_{GG}\overline{\overline{\Lambda}}_{GG}^{T}\right]^{-1} \\ \cdot\left[j\omega\overline{\overline{L}}_{GH}+\dfrac{1}{j\omega}\overline{\overline{\Lambda}}_{GG}\overline{\overline{Mat}}_{GG}\overline{\overline{\Lambda}}_{HG}^{T}\right] \\ -\overline{\overline{Mat}}_{GG}^{-1}\overline{\overline{K}}_{GH}\overline{\overline{K}}_{HH}^{-1}\overline{\overline{Mat}}_{GG}\overline{\overline{\Lambda}}_{HG}^{T} \end{array}\right\}\cdot\overline{i}_H \tag{37}$$

$$\overline{D}_3\left\{\overline{\phi}_H\right\}=\left\{\begin{array}{c} -\left[j\omega\overline{\overline{L}}_{HG}+\frac{1}{j\omega}\overline{\overline{\Lambda}}_{HG}\overline{\overline{Mat}}_{GG}\overline{\overline{\Lambda}}_{GG}^{T}\right] \\ \cdot\left[j\omega\overline{\overline{L}}_{GG}+\frac{1}{j\omega}\overline{\overline{\Lambda}}_{GG}\overline{\overline{Mat}}_{GG}\overline{\overline{\Lambda}}_{GG}^{T}\right]^{-1} \\ \cdot\left[\overline{\overline{\Lambda}}_{GH}+\overline{\overline{\Lambda}}_{GG}\overline{\overline{K}}_{GH}\overline{\overline{K}}_{HH}^{-1}\right]+\overline{\overline{\Lambda}}_{HG}\overline{\overline{K}}_{GH}\overline{\overline{K}}_{HH}^{-1} \end{array}\right\}\cdot\overline{\phi}_H \tag{38}$$

$$\overline{D}_4\left\{\bar{i}_H\right\}=\left\{\begin{array}{c} \frac{1}{\omega^2}\overline{\overline{\Lambda}}_{HG}\overline{\overline{Mat}}_{GG}\overline{\overline{\Lambda}}_{HG}^{T} \\ +\left[\overline{\overline{L}}_{HG}-\frac{1}{\omega^2}\overline{\overline{\Lambda}}_{HG}\overline{\overline{Mat}}_{GG}\overline{\overline{\Lambda}}_{GG}^{T}\right] \\ \cdot\left[\overline{\overline{L}}_{GG}-\frac{1}{\omega^2}\overline{\overline{\Lambda}}_{GG}\overline{\overline{Mat}}_{GG}\overline{\overline{\Lambda}}_{GG}^{T}\right]^{-1} \\ \cdot\left[\overline{\overline{L}}_{GH}-\frac{1}{\omega^2}\overline{\overline{\Lambda}}_{GG}\overline{\overline{Mat}}_{GG}\overline{\overline{\Lambda}}_{HG}^{T}\right] \end{array}\right\}\cdot\bar{i}_H \tag{39}$$

where

$$\overline{\overline{Mat}}_{HH}=\overline{\overline{K}}_{HH}-\overline{\overline{K}}_{HG}\overline{\overline{K}}_{GG}^{-1}\overline{\overline{K}}_{GH} \tag{40}$$

$$\overline{\overline{Mat}}_{GG}=\overline{\overline{K}}_{GG}-\overline{\overline{K}}_{GH}\overline{\overline{K}}_{HH}^{-1}\overline{\overline{K}}_{HG} \tag{41}$$

and the potential coefficient matrices $\overline{\overline{K}}_{HH}$, $\overline{\overline{K}}_{HG}$, $\overline{\overline{K}}_{GH}$ and $\overline{\overline{K}}_{GG}$ as well as the inductance matrices $\overline{\overline{L}}_{HH}$, $\overline{\overline{L}}_{HG}$, $\overline{\overline{L}}_{GH}$ and $\overline{\overline{L}}_{GG}$ are the partial element matrices obtained from MPIE method.

Step 3: use the perturbation method to calculate the cable harness current distributions iteratively.

Step 3.1: calculate the initial current distributions ($n=0$). Only the excitation terms $\left[-\,\bar{I}_H^{e\,T}\;\; \bar{v}_H^{e\,T}\right]^T$ on the right-hand side of (28) are included in the calculation and the correction terms are not considered.

$$\begin{bmatrix} j\omega\cdot \overline{\overline{K}}^{-1}_{HH,MTL} & \overline{\overline{\Lambda}}^{T}_{HH} \\ -\overline{\overline{\Lambda}}_{HH} & j\omega\cdot\overline{\overline{L}}_{HH,MTL}\end{bmatrix}\cdot\begin{bmatrix}\overline{\phi}_{H(0)}\\ \bar{i}_{H(0)}\end{bmatrix}=\begin{bmatrix}-\overline{I}^{e}_{H}\\ \overline{v}^{e}_{H}\end{bmatrix} \tag{42}$$

Step 3.2: calculate the corrected currents iteratively using the perturbation method ($n \geqslant 1$). Only the correction terms on the right-hand side of (28) are considered in the iterative calculations.

$$\begin{aligned}&\begin{bmatrix} j\omega\cdot \overline{\overline{K}}^{-1}_{HH,MTL} & \overline{\overline{\Lambda}}^{T}_{HH} \\ -\overline{\overline{\Lambda}}_{HH} & j\omega\cdot\overline{\overline{L}}_{HH,MTL}\end{bmatrix}\cdot\begin{bmatrix}\overline{\phi}_{H(n)}\\ \bar{i}_{H(n)}\end{bmatrix}= \\ &\qquad\begin{bmatrix} j\omega\cdot\overline{D}_1\left\{\overline{\phi}_{H(n-1)}\right\}+\overline{D}_2\left\{\bar{i}_{H(n-1)}\right\}+\overline{D}_5\left\{\bar{i}_{H(n-1)}\right\} \\ \overline{D}_3\left\{\overline{\phi}_{H(n-1)}\right\}+j\omega\cdot\overline{D}_4\left\{\bar{i}_{H(n-1)}\right\}+j\omega\cdot\overline{D}_6\left\{\bar{i}_{H(n-1)}\right\}\end{bmatrix}\end{aligned} \tag{43}$$

Step 3.3: determine if the calculated current distribution results have converged or not. Using the perturbation method, the current distributions on the cable harness can be calculated by

$$\bar{i}_H=\sum_{n=0}\bar{i}_{H(n)} \tag{44}$$

and the update of solved cable harness current at the n^{th} iteration is $\bar{i}_{H(n)}$:

$$\bar{i}_{H,new}=\bar{i}_{H,old}+\bar{i}_{H(n)} \tag{45}$$

If the maximum modification in the solved cable harness current at the current iteration step is smaller than the pre-set threshold value, the updates on the solved results are small enough and the perturbation calculation has converged. If the perturbation calculation has not converged and the modifications on the solved currents still have large corrections at current iteration step, the algorithm will go back to *Step 3.2* and calculate the next step of iteration ($n+1$).

5. NUMERICAL EXAMPLES

The method to solve the current distributions in a cable harness system using the improved Multiple Scattering method has been proposed in the previous section, and the improved Multiple Scattering method has only one iteration calculations after the improvement using the sub-structure analysis.

In this section, the effectiveness of the improved Multiple Scattering method is demonstrated using numerical examples. A four-wire MTL system with a slotted metal plane beneath the wires is shown in Figure 4 and Figure 5.

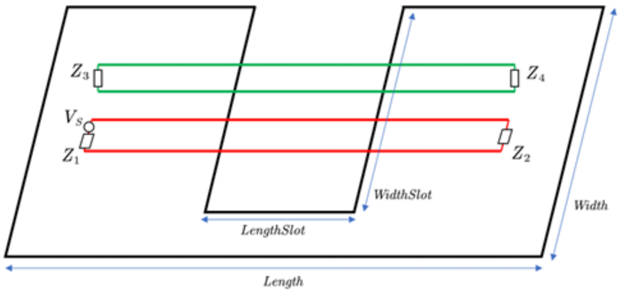

Figure 4. The four-wire system with a slotted metal plane beneath the wires.

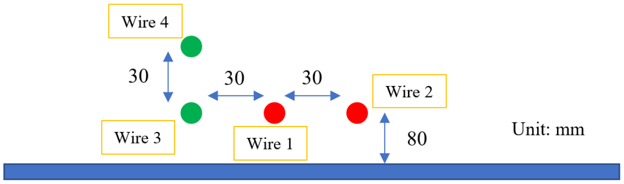

Figure 5. The cross-section of the four-wire system with a slotted metal plane beneath the wires.

There are two loops in the four-wire system, and there is only an excitation on the loop consisting of Wire 1 and Wire 2, which is marked in red color. This is the aggressor loop in the system. The other loop consisting of Wire 3 and Wire 4 (marked in green color) has no excitations on it and it is the victim loop in the system. All the current responses on the victim are resulted from the coupling from the aggressor loop. Resistive loadings with 0.1-Ohm resistance are added at all for terminals of the cable harness system, and a 1-V voltage source is added with the load Z_1 at one terminal of the aggressor loop, as shown in Figure 4. The length of each wire is 1.5 m, and the first resonant frequency of this system is 100 MHz. The length of the metal plane is 2.2 m and width of the plane is 0.8 m. And the slot is in the middle of the plane with the length and width of 0.4 m and 0.6 m, respectively.

The cross-sectional geometry of the four-wire system is shown in Figure 5. The distance between wires is 30 mm, and the distance between the cable harness system and the metal plane beneath is 80 mm.

Using the improved Multiple Scattering method to calculate the current distributions on the cable harness system at a non-resonant frequency (50 MHz), the calculated results on the aggressor loop is shown in Figure 6, and the results on the victim loop is shown in Figure 7. The results are also compared with the full-wave MoM results. In both Figure 6 and Figure 7, the red curves are the calculated current distributions using the full-wave MoM results; the thick dashed blue curves are the results from the improved Multiple Scattering method using the sub-structure analysis and generalized MTL methods; the thin dashed blue curves are the initial results in the Multiple scattering method before corrections using the iterative perturbation method.

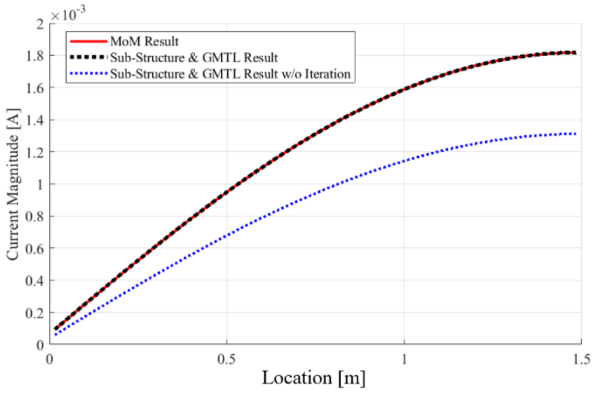

Figure 6. The current magnitudes comparison on the aggressor loop.

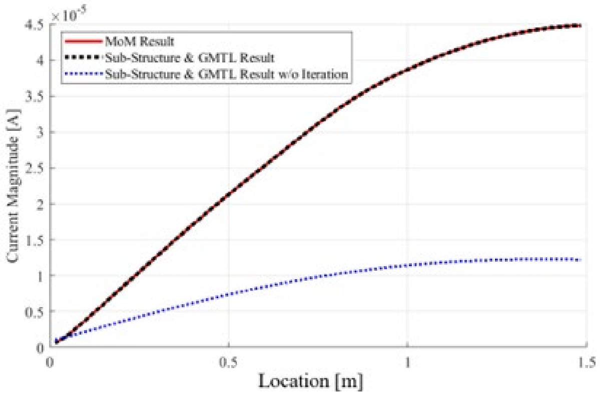

Figure 7. The current magnitudes comparison on the victim loop.

The current distributions on both the aggressor loop and the victim loop have good agreement to the full-wave MoM results. Without the corrections using the iterative perturbation method in the Multiple Scattering method, the current distributions have a smooth trend and are similar to an ideal MTL system. However, with the corrections through the iterative calculations, the discrepancies on the current distributions in both the aggressor loop and the victim loop can be corrected.

Then, the distance between the cable harness and the slotted metal plane is reduced from 80 mm to 40 mm, and the new geometry of the cross section is shown in Figure 8. After reducing the distance between the cable harness and the metal plane, the coupling between them should be stronger, and larger corrections are expected from the iterative calculations in the Multiple Scattering method.

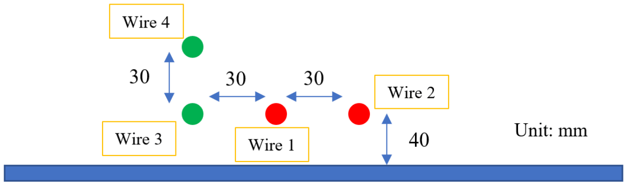

Figure 8. The cross-section of the four-wire system with a slotted metal plane beneath the wires and the distance between the metal and cable harenss is reduced to 40 mm.

The current distributions on the aggressor loop and the victim loop at the same frequency (50 MHz) are shown in Figure 9 and Figure 10, respectively.

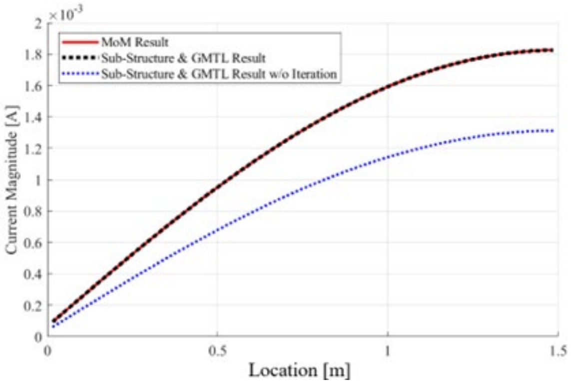

Figure 9. The current magnitudes comparison on the aggressor loop.

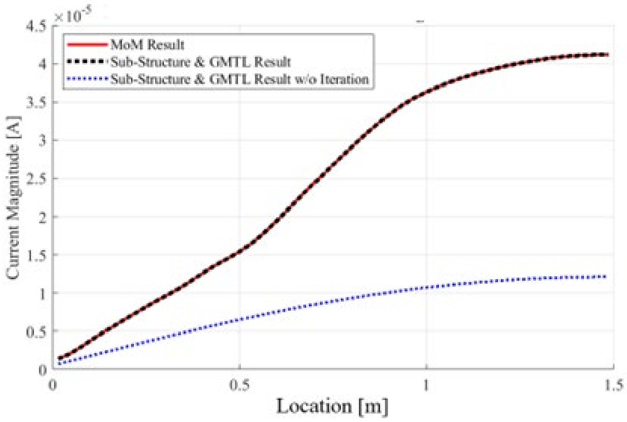

Figure 10. The current magnitudes comparison on the victim loop.

The observations on the current magnitudes comparisons on the aggressor loop and the victim loop are similar to the observations in the previous example where the distance between the cable harness and the metal plane is larger. Also, when the distance between the cable harness and the slotted metal plane becomes smaller and the coupling between them becomes stronger, the non-ideal MTL-like current distributions on the victim loop (changing of the slope of the current distribution curve) can also be caught using the improved Multiple Scattering method.

These two examples prove that the improved Multiple Scattering method is capable of correcting the calculated the current distributions on cable harness system with nearby metal surfaces, and the calculation algorithm is simplified using the sub-structure analysis.

However, in these two examples, the solution frequency is a non-resonant frequency of the cable harness system, and it has been discovered that the generalized MTL method is more likely to have convergence issue near the resonant frequencies of the system [11, 13]. In the improved Multiple Scattering method, the similar issue is also likely to happen, and the discussions on the convergence characteristics of the Multiple Scattering method are discussed in the following section.

6. DISCUSSION ON THE CONVERGENCE CHARACTERISTICS

The detailed explanation on the observation that the generalized MTL method is more difficult to converge near the resonant frequencies of a cable harness system is included in [11]. In short, near the resonant frequencies, the radiation behavior in the cable harness system becomes more dominant than the transmission-line behavior, so larger corrections are required from the perturbation calculations. However, the perturbation method is developed to correct a minor part of the differences in the solution, and if the part to be corrected is no longer a minor part, the perturbation method will not converge and the final solution from the perturbation method will be different to the expected explicit solution.

In the improved Multiple Scattering method, when the solution frequencies are closer to a resonant frequency of the cable harness system, the radiation behavior of the cable harness part will be stronger, and there will be stronger scattering fields between the cable harness and the nearby metal surfaces. Therefore, the correction terms in the Multiple Scattering method will also be larger and is likely to result in convergence issues in the iterative calculation.

For the same cable harness system shown in Figure 4 and Figure 8, calculate the current distributions at a resonant frequency of the cable harness system (100 MHz), and the comparisons on the calculation results are shown in Figure 11 and Figure 12.

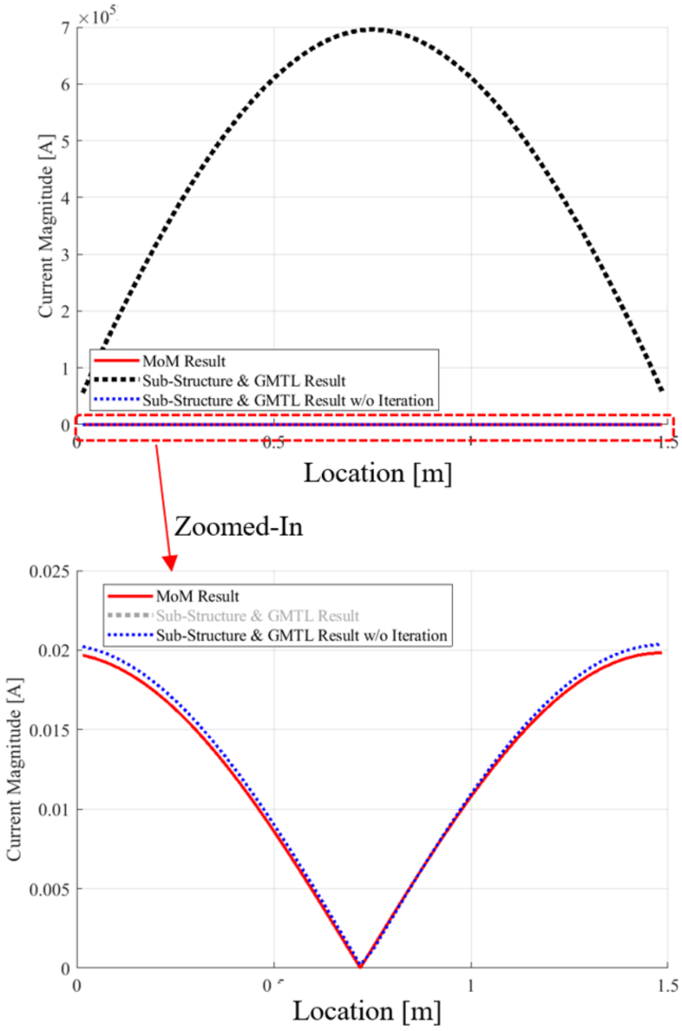

Figure 11. The current magnitudes comparison on the aggressor loop.

In Figure 11 and Figure 12, it can be observed that the calculated current distributions from the improved Multiple Scattering method are not converged on both the aggressor loop and the victim loop, and the calculated results have abnormal large values. In the zoomed-in view of Figure 11 and Figure 12, the discrepancies between the initial calculation in the improved Multiple Scattering method are larger on the victim loop compared to the aggressor loop, and the perturbation calculations make the discrepancies to the full-wave MoM results larger and larger during the iterations. These observations are typical behavior when the non-convergence issue happens in the perturbation method.

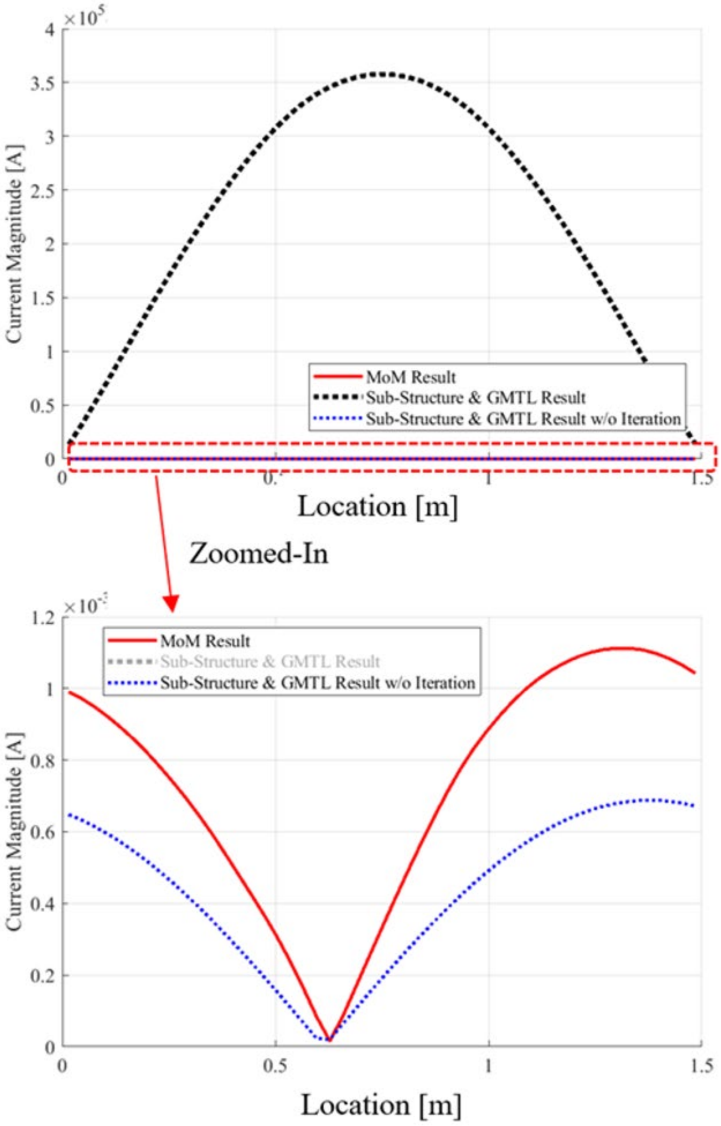

Figure 12. The current magnitudes comparison on the victim loop.

Then, the current distributions at the resonant frequency 100 MHz are calculated again in another modified cable harness system. In the modified system, the distance between the cable harness and the metal surface is increased from 40 mm to 140 mm. After increasing the distance between the cable harness and the metal surface, the coupling between them is expected to be weaker, and the perturbation method is more likely to converge in the modified system. The cross-sectional geometry of the modified cable harness system is shown in Figure 13, and the comparisons on the current distributions at 100 MHz of the modified model are shown in Figure 14 and Figure 15.

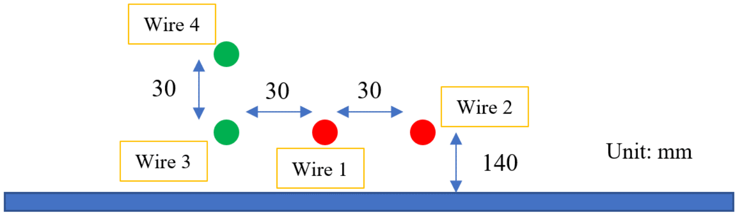

Figure 13. The cross-section of the four-wire system with a slotted metal plane beneath the wires and the distance between the metal and cable harenss is increased to 140 mm.

The comparisons shown in Figure 14 and Figure 15 indicate that the Multiple Scattering method converge at the resonant frequency (100 MHz). Also, because the coupling between the cable harness system and the metal surface becomes weaker, the discrepancies between the initial results in the improved Multiple Scattering method and the full-wave MoM results are smaller, meaning that less amounts of corrections are needed from the iterative calculations in the perturbation method. Thus, the iterative calculations are easier to converge.

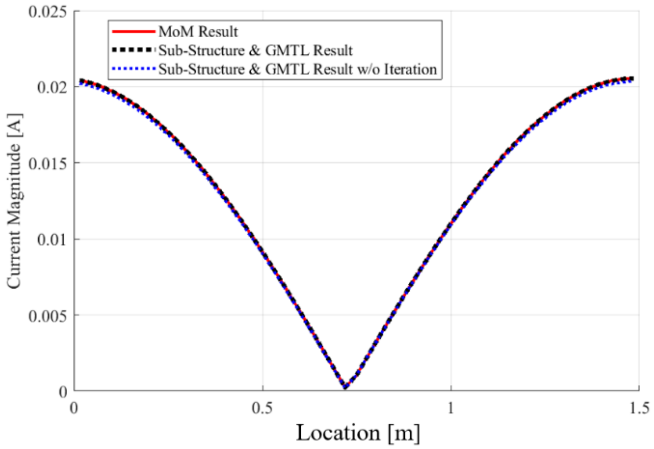

Figure 14. The current magnitudes comparison on the aggressor loop.

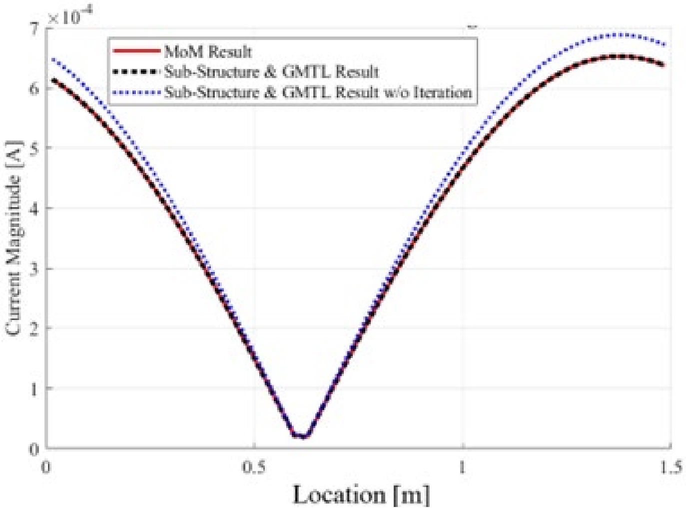

Figure 15. The current magnitudes comparison on the victim loop.

These observations on the convergence behavior are consistent with the expectations: near the resonant frequencies of the cable harness system, the perturbation method is more likely to have non-convergence behavior in the improved Multiple Scattering method; when the coupling between the cable harness and the nearby surfaces is mitigated, the iterative calculations in the improved Multiple Scattering method can have better convergence behavior.

In [11], a criterion is proposed to determine if the iterative calculations in the generalized MTL method is converged or not. The improved Multiple Scattering method uses the similar perturbation method as the generalized MTL method, so a similar criterion can be developed to evaluate if the improved Multiple Scattering method will converge or not before the iterative calculation starts.

Let the correction terms on the right-hand side of (28) be:

$$\begin{bmatrix} j\omega \cdot \overline{D}_1\left\{\overline{\phi}_H\right\} + \overline{D}_2\left\{\overline{i}_H\right\} + \overline{D}_5\left\{\overline{i}_H\right\} \\ \overline{D}_3\left\{\overline{\phi}_H\right\} + j\omega \cdot \overline{D}_4\left\{\overline{i}_H\right\} + j\omega \cdot \overline{D}_6\left\{\overline{i}_H\right\} \end{bmatrix} = \overline{\overline{\varepsilon}} \cdot \begin{bmatrix} \overline{\phi}_H \\ \overline{i}_H \end{bmatrix} \tag{46}$$

Then, the criterion of the convergence characteristics of the improved Multiple Scattering method can be written as:

$$\rho\left(\begin{bmatrix} j\omega \cdot \overline{\overline{K}}_{HH}^{-1} & \overline{\overline{\Lambda}}_{HH}^{T} \\ -\overline{\overline{\Lambda}}_{HH} & j\omega \cdot \overline{\overline{L}}_{HH} \end{bmatrix} \cdot \overline{\overline{\varepsilon}}\right) < 1 \tag{47}$$

where $\rho\left(\overline{\overline{A}}\right)$ indicates the spectral radius of the matrix $\overline{\overline{A}}$, which is the maximum eigenvalues of the matrix $\overline{\overline{A}}$.

Table 1. The Values of the Spectral Radius at 50 MHz and 100 MHz

Frequency [MHz]	50	100
Spectral Radius in the Improved Multiple Scattering Method	0.3725	2.563

In the numerical example shown in Figure 8 where the distance between the cable harness and the slotted surface is 40 mm, the value of the spectral radius at 50 MHz and 100 MHz are shown in Table 1. The results of spectral radius values are consistent with the observations on the convergence characteristics that the improved Multiple Scattering method converges at 50 MHz and does not converge at 100 MHz.

7. CONCLUSION

In this study, an improvement on the Multiple Scattering method for evaluating current distributions on cable harness system with nearby metal surfaces has been made with the help of the sub-structure analysis method. The proposed improved Multiple Scattering method is capable of correcting the discrepancies between the transmission-line results and the full-wave MoM results through iterative calculations in the perturbation method as the previous Multiple Scattering method, but the iterative steps in the improved Multiple Scattering method are simplified. The iterative calculations for the scattering between the cable harness and the nearby surfaces are merged together with the iterative calculations in the generalized MTL steps. In addition, the convergence characteristics of the improved Multiple Scattering method are discussed. Near the resonant frequencies of the cable harness system and with strong coupling between the cable harness and the nearby surfaces, the improved Multiple Scattering method would have higher risks on the non-convergence behavior, and the criterion to determine the convergence characteristics of the Multiple Scattering calculations are introduced.

REFERENCES

[1] D. Liu, Y. Wang, R. W. Kautz, N. Altunyurt, S. Chandra and J. Fan, "Accurate Evaluation of Field Interactions Between Cable Harness and Vehicle Body by a Multiple Scattering Method," in *IEEE Transactions on Electromagnetic Compatibility*, vol. 59, no. 2, pp. 383-393, April 2017.

[2] H. Bagci, A. E. Yilmaz, J. -M. Jin and E. Michielssen, "Fast and Rigorous Analysis of EMC/EMI Phenomena on Electrically Large and Complex Cable-Loaded Structures," in *IEEE Transactions on Electromagnetic Compatibility*, vol. 49, no. 2, pp. 361-381, May 2007.

[3] Y. Guo *et al.*, "High-Frequency Modeling of Permanent Magnet Synchronous Motor Considering Internal Imbalances," *2021 Asia-Pacific International Symposium on Electromagnetic Compatibility (APEMC)*, Nusa Dua - Bali, Indonesia, 2021, pp. 1-3.

[4] M. Ouyang, X. Wang, N. Altunyurt, V. Sanphuang, N. Parsa and J. Fan, "Cable Harness Modeling Using MTL Parameters Derived from Integral Equations," *2020 IEEE International Conference on Computational Electromagnetics (ICCEM)*, Singapore, 2020, pp. 66-68.

[5] D. Zhang, Y. Wen, Y. Wang, D. Liu, X. He and J. Fan, "Coupling Analysis for Wires in a Cable Tray Using Circuit Extraction Based on Mixed-Potential Integral Equation Formulation," in *IEEE Transactions on Electromagnetic Compatibility*, vol. 59, no. 3, pp. 862-872, June 2017.

[6] Y. Wang *et al.*, "Evaluating Field Interactions Between Multiple Wires and the Nearby Surface Enabled by a Generalized MTL Approach," in *IEEE Transactions on Electromagnetic Compatibility*, vol. 60, no. 4, pp. 971-980, Aug. 2018.

[7] F. Middelstaedt, S. V. Tkachenko, R. Rambousky and R. Vick, "High-Frequency Electromagnetic Field Coupling to a Long, Finite Wire With Vertical Risers Above Ground," in *IEEE Transactions on Electromagnetic Compatibility*, vol. 58, no. 4, pp. 1169-1175, Aug. 2016.

[8] Y. Leviatan and A. T. Adams, "The Response of a Two-Wire Transmission Line to Incident Field and Voltage Excitation, Including the Effects of Higher Order Modes," *1981 IEEE International Symposium on Electromagnetic Compatibility*, Boulder, CO, USA, 1981, pp. 1-8.

[9] Clayton R. Paul, “Restrictions on the Applicability of the Transmission-Line Equation Formulation,” in *Analysis of Multiconductor Transmission Lines, 2nd* ed. City of Publisher, New Jersey, USA: John Wiley & Sons, 2007, ch. 1, sec. *5*, pp. 37–47.

[10] Y. Wang, Y. S. Cao, D. Liu, R. W. Kautz, N. Altunyurt and J. Fan, "A Generalized Multiple-Scattering Method for Modeling a Cable Harness With Ground Connections to a Nearby Metal Surface," in *IEEE Transactions on Electromagnetic Compatibility*, vol. 61, no. 1, pp. 261-270, Feb. 2019.

[11] M. Ouyang *et al.*, “Improvement of Convergence Characteristics in the Generalized Multiconductor Transmission-Line Method Near Resonant Frequencies,” submitted to IEEE Transactions on Signal and Power Integrity.

[12] J. Ethier and D. A. McNamara, “Sub-structure characteristic mode concept for antenna shape synthesis,” *Electron. Lett.*, vol. 48, no. 9, pp. 471-472, 2012.

[13] Y. Wang, Y. S. Cao, D. Liu, R. W. Kautz, N. Altunyurt and J. Fan, "Evaluating the Crosstalk Current and the Total Radiated Power of a Bent Cable Harness Using the Generalized MTL Method," in *IEEE Transactions on Electromagnetic Compatibility*, vol. 62, no. 4, pp. 1256-1265, Aug. 2020.

[14] S. Chabane, P. Besnier and M. Klingler, "Enhanced transmission line theory: Frequency-dependent line parameters and their insertion in a classical transmission line equation solver," *2013 International Symposium on Electromagnetic Compatibility*, Brugge, Belgium, 2013, pp. 326-331.

[15] S. Chabane, P. Besnier and M. Klingler, "A Modified Enhanced Transmission Line Theory Applied to Multiconductor Transmission Lines," in *IEEE Transactions on Electromagnetic Compatibility*, vol. 59, no. 2, pp. 518-528, April 2017.

SECTION

2. CONCLUSIONS

This dissertation presents the approach to improve the convergence characteristics of the generalized MTL method near the resonant frequencies of a cable harness system. By introducing the additional radiation loss resistances into the original MTL matrix, less corrections from the perturbation method are required and the generalized MTL method is easier to converge. Also, the Multiple Scattering method for cable harness current distribution evaluation is improved with the sub-structure analysis method. The iteration steps in the original Multiple Scattering method are simplified, and the convergence characteristics of the improved Multiple Scattering method are discussed.

In addition, the multiple reflections in a cascaded high-speed channel are investigated, and the method has been developed to optimize the single-bit response and the eye diagram opening by identifying the critical wave components reflecting in the cascaded channel and backtracking their propagation path. A better understanding on the multiple reflections in a cascaded channel can be obtained from the analytical formulations, and the channel response is able to be optimized more efficiently.

.

VITA

Muqi Ouyang was born in Wuhan, Hubei Province, P.R. China. In May 2016, he received his degree of bachelor's in electrical engineering and Automation in Huazhong University of Science and Technology, Wuhan, Hubei Province, P.R. China.

He started his M.S. program in August 2016 at Missouri University of Science and Technology and converted to Ph.D. program in August 2017. He worked in Missouri S&T EMC Laboratory and his research interests included signal integrity, electromagnetic interferene, radio-frequency interference, and computational electromagnetics. In December 2022, he received his Ph.D degree in Electrical Engineering from Missouri University of Science and Technology.